

# Wildfire smoke triggers cirrus formation: Lidar observations over the Eastern Mediterranean (Cyprus)

Rodanthi-Elisavet Mamouri<sup>1,4</sup>, Albert Ansmann<sup>2</sup>, Kevin Ohneiser<sup>2</sup>, Daniel A. Knopf<sup>3</sup>, Argyro Nisantzi<sup>1,4</sup>, Johannes Bühl<sup>5</sup>, Ronny Engelmann<sup>2</sup>, Annett Skupin<sup>2</sup>, Patric Seifert<sup>2</sup>, Holger Baars<sup>2</sup>, Dragos Ene<sup>1</sup>, Ulla Wandinger<sup>2</sup>, and Diofantos Hadjimitsis<sup>1,4</sup>

<sup>1</sup>Eratosthenes Centre of Excellence, Limassol, Cyprus

<sup>2</sup>Leibniz Institute for Tropospheric Research, Leipzig, Germany

<sup>3</sup>School of Marine and Atmospheric Sciences, Stony Brook University, Stony Brook, NY 11794-5000, USA

<sup>4</sup>Cyprus University of Technology, Dep. of Civil Engineering and Geomatics, Limassol, Cyprus

<sup>5</sup>Technical University Wernigerode, Wernigerode, Germany

**Correspondence:** R. E. Mamouri (rodanthi.mamouri@eratosthenes.org.cy), A. Ansmann (albert@tropos.de)

## Abstract.

The number of intense wildfires may further increase in the upcoming years as a consequence of climate change. It is therefore necessary to improve our knowledge about the role of smoke in the climate system with emphasis on the impact of smoke particles on the evolution of clouds, precipitation, and cloud radiative properties. Presently, one key aspect of research is whether or not wildfire smoke particles can initiate cirrus formation. In this study, we present lidar observations over Limassol, Cyprus, from 27 October to 3 November 2020 when extended wildfire smoke fields crossed the Mediterranean Basin from Portugal to Cyprus. We found strong evidence that aged smoke particles (organic aerosol particles) originating from wildfires in North America triggered significant ice nucleation at temperatures from  $-47$  to  $-53^{\circ}\text{C}$  and caused the formation of extended cirrus layers. The observations suggest that the ice crystals were nucleated just below the tropopause in the presence of smoke particles serving as ice-nucleating particles (INPs). The main part of the 2-3 km thick smoke layer was, however, in the lower stratosphere just above the tropopause. With actual radiosonde observations of temperature and relative humidity and lidar-derived smoke particle surface area concentrations as starting values, gravity wave simulations show that lofting of air by 100-200 m is sufficient to initiate significant ice nucleation on the smoke particles, expressed in ice crystal number concentrations of  $1\text{-}100\text{ L}^{-1}$ .

## 1 Introduction

Record-breaking wildfires in western Canada (2017), southeastern Australia (2019-2020), and central Siberia (2019) caused strong perturbations of the aerosol conditions in the upper troposphere and lower stratosphere (UTLS) (Baars et al., 2019; Kloss et al., 2019; Ohneiser et al., 2021, 2022; Rieger et al., 2021). Smoke was lofted by pyrocumulonimbus (pyroCb) convection (Peterson et al., 2018, 2021) or self-lofting processes (Ohneiser et al., 2021, 2023) into the UTLS height range, was transported around the globe, and polluted large parts of the northern and southern hemisphere from the subtropics to the poles over months. Recent studies suggest that major fire-related hemispheric perturbations may become more frequent in the future within a

changing global climate with more hot and dry weather periods (Jolly et al., 2015; Abatzoglou et al., 2019; Kirchmeier-Young et al., 2019). Besides extraordinarily intense fire storms, numerous small to moderate wildfires and biomass burning events all over the world serve as a persistent source of smoke particles in the free troposphere (Mattis et al., 2008; Dahlkötter et al., 2014; Burton et al., 2015; Vaughan et al., 2018; Foth et al., 2019; Floutsi et al., 2021; Veselovskii et al., 2022). Based on airborne pole-to-pole in situ aerosol observations during the Atmospheric Tomography (ATom) mission, Schill et al. (2020) found that biomass burning particles are diluted but ubiquitous accounting for one-quarter of the accumulation-mode number in the remote free troposphere up to tropopause heights.

To be able to adequately consider fresh and aged wildfire smoke in global chemistry and climate models (Hodzic et al., 2020), the role of smoke particles in the atmospheric system needs to be explored in more detail by means of satellite remote sensing, field observations (in situ, remote sensing), with laboratory experiments, and cloud-resolving atmospheric modeling on regional to global scales. An open question is to what extent wildfire smoke particles are able to serve as ice-nucleating particles (INPs) in heterogeneous ice formation processes and thus to influence the occurrence frequency and development of mixed-phase and cirrus clouds, and in this way the hydrological cycle and radiative transfer in the atmosphere. The few available observations show so far that wildfire smoke particles seem to be inefficient INPs in mixed-phase cloud processes with temperatures of  $> -35^{\circ}\text{C}$  (see, e.g., Barry et al., 2021). Similarly, Froyd et al. (2010) found no indication that wildfire smoke particles influence cirrus formation.

In this article, we show the opposite. We found clear evidence for an impact of aged wildfire smoke on cirrus formation in lidar observations over the Eastern Mediterranean in October-November 2020. The smoke originated from record-breaking Californian wildfires (Safford et al., 2022). Almost 10000 fires had burned more than 4% of California's roughly 100 million acres of land in 2020. The 2020 fire period was the largest and strongest recorded fire season in the history of California. Lofted layers of aged smoke from these fires were observed over the North Pole (Ansmann et al., 2023), central Europe (Baars et al., 2021; Hu et al., 2022), and over the Mediterranean Basin (Michailidis et al., 2023) from September to November 2020. Continuous ice nucleation just below the tropopause at temperatures from  $-46^{\circ}$  to  $-52^{\circ}\text{C}$  was monitored at Limassol, Cyprus, in smoke-burden air from 27 October to 3 November 2020. It should be emphasized here that such events of aerosol-cirrus interaction as presented in this article remain probably undetected if a continuously running lidar is not available. Only lidar (comparable with a running camera) allows us to monitor aerosol conditions and cirrus evolution at the same time with the required high temporal and vertical resolution. The Limassol observations corroborate our opinion.

This was not the first time that we found a strong link between smoke occurrence and cirrus formation. During the MOSAiC (Multidisciplinary drifting Observatory for the Study of Arctic Climate) expedition (Engelmann et al., 2021; Ohneiser et al., 2021; Ansmann et al., 2023) we detected Siberian smoke in the UTLS height range for more than seven months (October 2019 to May 2020). Numerous cirrus fields developed via heterogeneous ice nucleation on the smoke particles over the high Arctic ( $85^{\circ}$ - $88^{\circ}\text{N}$ ) as the combined lidar-radar data analysis revealed. Furthermore, the preliminary analysis of our smoke observations at Punta Arenas, in southern Chile, point also to a strong impact of wildfire smoke on cirrus formation in January-April 2020. The smoke over the southernmost tip of South America originated from the record-breaking Australian bushfires around New Year 2020 (Ohneiser et al., 2020, 2022).

The impact of biomass burning aerosol on ice nucleation is complex, and this fact will make the implementation of smoke into cloud-process-resolving simulation models rather difficult. Ansmann et al. (2021) and Hu et al. (2022) provide brief overviews about smoke properties and smoke aging processes during long range transport with focus on aged free tropospheric and UTLS smoke layers observable with lidar. It seems that aged smoke particles in the UTLS height range typically show a compact core-shell structure with a black-carbon-containing core and an organic-material-rich shell (Dahlkötter et al., 2014). With increasing compactness (towards the formation of a spherical shape) of the smoke particles the linear depolarization ratio, measured with lidar, decreases with time, sometimes within hours to days, sometimes rather slowly over weeks to months (Baars et al., 2019; Ohneiser et al., 2022).

Smoke particles can occur as glassy, semi-solid, and liquid aerosol particles. As a consequence of the complex chemical and morphological properties, the development of smoke INP parameterization schemes is a crucial task (Knopf et al., 2018; Knopf and Alpert, 2023). The ability to serve as INP mainly depends on the material in the particle's shell (Charnawskas et al., 2017). Several studies indicate that aged smoke particles from forest fires contain only 2-3% black carbon (BC) (Dahlkötter et al., 2014; Mardi et al., 2018; Yu et al., 2019; Torres et al., 2020; Ohneiser et al., 2023) so that the organic substances (organic carbon, OC) are responsible for the ice nucleation activity. Biomass-burning particles also contain humic like substances (HULIS) which represent large macromolecules that may serve as INP at low temperatures of  $-50$  to  $-70^{\circ}\text{C}$  (Wang and Knopf, 2011; Knopf et al., 2018). If the particles are in a glassy state, they can serve as deposition ice nucleation (DIN) particles (Zobrist et al., 2008; Murray et al., 2010; Wang et al., 2012a; Berkemeier et al., 2014; Knopf et al., 2018). DIN is defined as ice formation occurring on the INP surface by water vapor deposition from the supersaturated gas phase. DIN could be the result of pore condensation freezing (Marcolli, 2014; Knopf and Alpert, 2023). When the smoke particles take up supercooled water and their shell deliquesces, immersion freezing can proceed, where the remaining solid part of the particle (immersed in the liquid shell) serves as an INP. If the smoke particles completely dissolve and become liquid (and no insoluble material within the particles is left), homogeneous freezing will take place on the resulting aqueous solutions at temperatures below  $-38^{\circ}\text{C}$  (Knopf and Alpert, 2023).

Besides emission of gases and smoke particles, bottom ash and soil dust is injected into the atmosphere during fires (Nisantzi et al., 2014; Wagner et al., 2018) and may reach the upper troposphere. Dust and ash particles are known to be efficient INPs at cirrus temperatures (Seifert et al., 2010, 2011; DeMott et al., 2015; Kilchhofer et al., 2021; Froyd et al., 2022). Based on laboratory studies, Jahn et al. (2020) also show that the combustion process transforms inorganic elements naturally present in the biomass (not soil or dust) to form potentially ice-active minerals in both the bottom ash and emitted aerosol particles. These particles possess ice-nucleation activities high enough to be relevant to mixed-phase clouds and are active over a wide temperature range, nucleating ice at up to  $-13^{\circ}\text{C}$ . Jahn et al. (2020) and Jahl et al. (2021) hypothesized that these mineral components are mainly responsible for the ice nucleation efficiency of wildfire smoke particles. We will include these aspects in the discussion of our observations in Sect. 4. We begin with information about the lidar stations at Limassol and the lidar data analysis in Sects. 2 and 3. The observations are presented and discussed in Sect. 4.

## 2.1 Cyprus Atmospheric Remote Sensing Observatory (CARO)

A multiwavelength polarization Raman lidar, Polly (POrtabLe Lidar sYstem) (Engelmann et al., 2016), was used to monitor smoke layers and cirrus clouds. It is operated at the Cyprus Atmospheric Remote Sensing Observatory (CARO) of the Eratosthenes Centre of Excellence at Limassol (34.677°N, 33.0375°E, 2.8 m above sea level, a.s.l.). A sunphotometer is operated in addition at Limassol since 2010 in the framework of AERONET (Aerosol Robotic Network, CUT-TEPAK station) (Holben et al., 1998; AERONET, 2023). One of the main research topics comprises the vertically resolved characterization of aerosols and the interaction between aerosols, clouds, precipitation, and atmospheric dynamics in the highly polluted Eastern Mediterranean where complex mixtures of desert and agricultural dust, biogenic particle components, and anthropogenic haze regularly occur (Mamouri et al., 2013, 2016; Nisantzi et al., 2014, 2015; Ansmann et al., 2019a; Radenz et al., 2021). CARO is part of the ACTRIS (Aerosols, Clouds and Trace gases Research InfraStructure) National Facility of the Republic of Cyprus for remote sensing of aerosols and clouds (ACTRIS, 2023).

## 2.2 Polly instrument and primary lidar data analysis

The setup and basic technical details of the Polly instrument are given in Engelmann et al. (2016), Hofer et al. (2017), and Jimenez et al. (2020). The diode-pumped laser transmits linearly polarized laser pulses at 355, 532, and 1064 nm with a pulse repetition rate of 100 Hz. All laser beams are tilted to an off-zenith angle of 5° to avoid ambiguous values of the measured optical properties of mixed-phase and cirrus clouds caused by specular reflection of falling, horizontally aligned hexagonal plates and columns (Thomas et al., 1990). When pointing to the zenith, specular reflections on the surfaces of horizontally oriented ice crystals (acting as mirrors) especially lead to very low particle linear depolarization, very close to zero (because this reflection does not change the laser light polarization). As a consequence, ice depolarization ratios from horizontally oriented ice crystals cannot be distinguished from the low depolarization ratios resulting from backscattering by spherical liquid-water droplets. Thus, to unambiguously identify the ice phase of a cloud layer, off-zenith observations are a basic requirement in cloud lidar research. Randomly oriented ice particles lead to linear depolarization ratios of typically 40–50% (produced by scattering and reflection processes within the ice crystals at many non-180° scattering and reflection angles), whereas liquid-water droplets cause values close to 0% and usually <20% in the case of multiple scattering in dense water cloud layers.

A detailed description of the Polly data analysis regarding particle optical properties can be found in Baars et al. (2016), Hofer et al. (2017), Jimenez et al. (2020), and Ohneiser et al. (2020, 2021, 2022). The polarization Raman lidar permits us to measure height profiles of the particle backscatter coefficient  $\beta$  at the laser wavelengths of 355, 532 and 1064 nm, particle extinction coefficient  $\alpha$  at 355 and 532 nm, the corresponding lidar ratios  $L = \alpha/\beta$ , and the volume and particle linear depolarization ratios at 355 and 532 nm. Uncertainties in the lidar products are about 5-15% (particle backscatter coefficient, linear depolarization ratio), and 5-30% (particle extinction coefficient, extinction-to-backscatter ratio).



We will especially make use of the height profiles of the 532 nm particle backscatter coefficients at smoke and cirrus height level. The so-called Klett-Fernald method (Klett, 1981; Fernald, 1984) allows us to determine profiles of the backscatter coefficient from strong elastic-backscatter signal profiles. That means the profiles can be obtained with high vertical and temporal resolution. However, the lidar ratio must be given as input and may cause large uncertainties (20-40% relative uncertainty). In contrast, the Raman lidar method (Ansmann et al., 1992) does not need critical input parameters, and thus is more accurate. However, this method is based on the analysis of height profiles of the ratio of the elastic-backscatter signal to the respective Raman signal. To keep the influence of enhanced signal-to-noise low, longer vertical smoothing and longer signal averaging times are required when using this method.

### 130 2.3 Nicosia radiosonde station

The Athalassa Radiosonde Station 17607 (35.14°N, 33.39°E, 160 m a.s.l.), Nicosia, Cyprus launches two Vaisala RS41-SGP radiosondes daily, at 05:00 and 11:00 UTC. The sonde measures pressure, temperature, relative humidity, horizontal wind velocity and direction (Nicosia-Athalassa-RS, 2023). The Nicosia radiosonde station is 61.4 km northeast of the Limassol CARO site.

## 135 3 Lidar data analysis

The POLIPHON (POLarization LIdar PHOTometer Networking) method (Mamouri and Ansmann, 2016, 2017) enables us to retrieve aerosol-type-dependent microphysical products from the measured height profiles of the particle backscatter coefficient and to estimate cloud-process-relevant properties such as CCN and INP concentrations. A detailed view on the POLIPHON potential regarding dust and wildfire smoke retrievals is given by Ansmann et al. (2019b, 2021).

140 In this study, we make use of the conversion of 532 nm backscatter coefficients into particle surface area concentration  $s$  and particle number concentration  $n_{250}$  (number concentration of particles with radius  $>250$  nm).  $s$  is the smoke input parameter in the INP parameterization, described in the next section, and  $n_{250}$  indicates the number of particles that could potentially be activated as INP. In the case of mineral dust,  $n_{250}$  is used as aerosol input in INP estimations by DeMott et al. (2015).

The following relationships are used to calculate  $s$  and  $n_{250}$  (Mamouri and Ansmann, 2017; Ansmann et al., 2021):

$$145 \quad s(z) = c_s L \beta(z), \quad (1)$$

$$n_{250}(z) = c_{250} L \beta(z) \quad (2)$$

with the 532 nm particle backscatter coefficient  $\beta(z)$  at height  $z$  and the extinction-to-backscatter or lidar ratio  $L$ . For the wildfire smoke episode in October 2020, we measured smoke lidar ratios of around 75 sr as shown in Sect. 4.1. Lidar ratios of  $>70$  sr are indicative for strongly light-absorbing smoke particles (Haarig et al., 2018; Ohneiser et al., 2020, 2022). The extinction-to-surface-area conversion factor  $c_s$  and the extinction-to-number conversion factor  $c_{250}$  for 532 nm are  $1.75 \text{ Mm } \mu\text{m}^2 \text{ cm}^{-3}$  and  $0.35 \text{ Mm cm}^{-3}$ , respectively (Ansmann et al., 2021). Considering an uncertainty of 25% in the conversion factors and a lidar ratio uncertainty of about 15-20%, we can obtain the microphysical properties with a relative uncertainty of about 30%.

These conversion factors for aged wildfire smoke are determined at dry aerosol conditions (Ansmann et al., 2021) and thus hold for dry aerosol particles. Since the  $s$  and  $n_{250}$  retrievals are based on lidar observations performed during cirrus free conditions, a potential bias (overestimation of dry particle backscatter and thus of  $s$  and  $n_{250}$ ) caused by water uptake by the smoke particles in the upper, usually dry troposphere is neglected here. The Nicosia radionsonde observations during our measurement period support this assumption. The relative humidity over water was  $<25\%$  during cirrus-free conditions and less than  $60\%$  during cirrus events, when the radiosondes ascended in obviously cirrus-free air. At these conditions, water uptake by smoke particles is of minor importance and the bias in the conversion  $<10\%$ .

### 160 3.1 INP parameterization

The estimation of INP concentrations is challenging due to the chemical complexity of smoke aerosol (Kanji et al., 2017; Knopf et al., 2018; Jahn et al., 2020). We assume that the ability of aged smoke particles to serve as INP mainly depends on the organic material of the particles and on the thermodynamic state (glassy, semi-solid, liquid) (Knopf et al., 2018). According to the simulations of Berkemeier et al. (2014), glassy states and solid/liquid core-shell morphologies can persist for long enough in typical atmospheric updrafts so that heterogeneous ice nucleation in the deposition and immersion mode can dominate over homogeneous ice nucleation. Such competition depends strongly on ambient temperature and relative humidity as well as humidification rate and particle size.

In the following, we briefly outline procedures to compute INP concentrations for immersion freezing and deposition ice nucleation. Knopf and Alpert (2013) introduced the water-activity-based immersion freezing model (ABIFM) and presented the respective parameterization for two types of humic compounds based on experimental data (Rigg et al., 2013). We chose to apply the ABIFM for Leonardite (a standard humic acid surrogate material) to represent the amorphous organic coating of smoke particles. The ABIFM allows the prediction of the ice particle production rate  $J_{\text{het}}^{\text{IF}}$  as a function of ambient air temperature  $T$  (freezing temperature) and ice supersaturation  $S_{\text{ICE}}$  (Knopf and Alpert, 2023). In the first step, the so-called water activity criterion is computed (Koop et al., 2000):

$$175 \quad \Delta a_w = a_w - a_{w,i}(T) \quad (3)$$

with the relative humidity over water RH in decimal numbers (e.g., 0.7 for RH=70%). RH equals condensed-phase water activity  $a_w$ , when particle and ambient RH are in equilibrium.  $a_{w,i}$  denotes the water activity at the ice melting point for a given aqueous solution and is expressed as the ratio of the ice saturation pressure  $p_i$  to water saturation pressure  $p_w$  as function of temperature  $T$  in the air parcel in which ice nucleation takes place. RH and temperature values may be available from radiosonde ascents or taken from data bases with re-analyzed global atmospheric data. In the next step, the ice crystal nucleation rate coefficient  $J_{\text{het}}^{\text{IF}}$  (in  $\text{cm}^{-2} \text{s}^{-1}$ ) is calculated:

$$180 \quad \log_{10}(J_{\text{het}}^{\text{IF}}) = b + k\Delta a_w. \quad (4)$$

The particle parameters  $b$  and  $k$  are determined from laboratory studies. For Leonardite,  $b$  is  $-13.4$  and  $k$  is  $66.9$  (Knopf and Alpert, 2013). In the final step, we obtain the number concentration of smoke INP for the immersion freezing mode,

$$185 \quad n_{\text{INP}}^{\text{IF}} = s J_{\text{het}}^{\text{IF}} \Delta t \quad (5)$$

with the particle surface area concentration  $s$  and the time period  $\Delta t$  (in seconds) during which  $T$  and  $S_{\text{ICE}}$  are constant. In our gravity wave simulation in Sect. 4.3, the time step is  $\Delta t = 10$  s (in simulations of waves with periods of 1200-1600 s).

We consider DIN as the main heterogeneous ice nucleation mode at typical cirrus temperatures  $< 230$  K (Murray et al., 2010; Chou et al., 2013; Kilchhofer et al., 2021). Wang and Knopf (2011) and Wang et al. (2012b) provide a simplified  
 190 parameterization of DIN, based on classical nucleation theory, that describes the DIN efficiency and the ice crystal nucleation rate coefficient  $J_{\text{het}}^{\text{DIN}}$  as a function of  $T$ ,  $S_{\text{ICE}}$ , and the ice-nucleation-relevant aerosol composition, e.g., humic and fulvic acid compounds. The procedure (for lidar applications) is outlined in Ansmann et al. (2021). The INP number concentration (or predicted ice crystal number concentration) is given by:

$$n_{\text{INP}}^{\text{DIN}} = s J_{\text{het}}^{\text{DIN}}(c_{\text{angle}}, T, S_{\text{ICE}}) \Delta t. \quad (6)$$

195 The ice nucleation rate coefficient  $J_{\text{het}}^{\text{DIN}}$  is a function of the contact angle  $c_{\text{angle}}$ . The selected contact angle is  $26.5^\circ$  in the wildfire smoke INP computation (Wang and Knopf, 2011). Though, for each species  $c_{\text{angle}}$  can range about  $7^\circ$ - $10^\circ$ . For the contact angle of  $26.5^\circ$ , the ice nucleation onset  $\text{RH}_{\text{ICE}}$  (relative humidity over ice) is around 140%.

The uncertainties in the computed INP concentrations are large (1-2 orders of magnitude). In view of these large uncertainties, it is necessary in the analysis of field observations to perform closure studies as presented by Ansmann et al. (2019a) and  
 200 Marinou et al. (2019). By combining observations, parameterization results, and simulations, the uncertainties in the individual results and in the overall product data set can be significantly reduced.

## 4 Observations and discussion

### 4.1 Smoke identification and optical characterization

From 21 October to 3 November 2020 extended North American wildfire smoke layers crossed the Mediterranean Basin from  
 205 Portugal to Cyprus between 6 and 14 km height (Michailidis et al., 2023). Lidar measurements at Evora, Portugal, and Potenza, Italy, documented this event on 24 and 26 October 2020, respectively. The smoke originated from large wildfires in California, USA, and traveled 8 days before reaching Europe. Figure 1 contains a smoke measurement with the Polly instrument at Cyprus on 27 October 2020 (PollyNET, 2023). Weak aerosol structures are visible from 6-11 km height, and pronounced layers were detected from 11-14 km height. In Fig. 2, backward trajectories confirm the 8-9 day long-range transport of smoke from the  
 210 western United States to the Eastern Mediterranean.

The strong wavelength dependence of the backscatter coefficient and the respectively high backscatter Ångström exponents of 1-2, and the weak wavelength dependence of the extinction coefficient are typical for aged, strongly light-absorbing wildfire smoke particles. In the optically thickest part from 12-13 km height with highest particle extinction coefficients, the lidar ratio

was about 70-90 sr at 532 nm and 50-60 sr at 355 nm. This inverse spectral dependence of the lidar ratio is characteristic for aged wildfire smoke (Haarig et al., 2018; Ohneiser et al., 2020, 2021). The main smoke layer was above the tropopause.

As mentioned in the introduction, bottom ash and soil dust may be components of the wildfire aerosol mixtures and thus may reach the upper troposphere as well. Dust and ash particles are known to be efficient INPs at cirrus temperatures (Seifert et al., 2010, 2011; DeMott et al., 2015; Kilchhofer et al., 2021; Froyd et al., 2022). However, the observed spectral dependence of the particle backscatter coefficient in Fig. 1b is typical for aged wildfire smoke particles. These particles form a pronounced accumulation-mode (Haarig et al., 2018; Ohneiser et al., 2020, 2022). Especially, the strong decrease of the backscatter coefficient from 532 to 1064 nm indicates that coarse-mode dust and ash particles were most probably absent.

The enhanced particle depolarization ratios of 0.1-0.15 at both wavelengths indicate non-spherical particles. The particles were probably lofted by pyroCb convection to the tropopause region. The fast lofting into the dry upper troposphere is assumed to prohibit fast aging of the particles, i.e., condensation of gases emitted over the fire places as well as of water vapor on the freshly emitted irregularly shaped particles, and thus the development of a perfect spherical core-shell structure (causing low depolarization ratios close to zero) (Haarig et al., 2018; Baars et al., 2019; Ohneiser et al., 2020; Ansmann et al., 2021). Lofting of smoke by pyroCbs up to the tropopause (at 13-14 km over California in October 2020) is, however, not considered in the HYSPLIT (Hybrid Single-Particle Lagrangian Integrated Trajectory model) simulations (Stein et al., 2015; Rolph et al., 2017). Thus, the trajectories in Fig. 2 can only be used to follow the smoke-polluted airmasses on their way towards Europe. Our analyses are in good agreement with the lidar measurements at Evora, Portugal, and Potenza, Italy, and the HYSPLIT backward trajectory analysis presented by Michailidis et al. (2023).

The particles were probably in a glassy state and showed an almost spherical solid/liquid core-shell morphology (Gialitaki et al., 2020). In the case of perfect spheres, the depolarization ratio would be 0.01-0.03. The PDLR values above 13 km result from smoothing of very noisy data and should be ignored.

## 4.2 Ice nucleation in wildfire smoke

On 28 and 30 October 2020, ice clouds developed at the tropopause over Cyprus. According to Figs. 3b and d, the main smoke layer was located between the tropopause and 12-12.5 km height on these two days. The sharp drop in the  $RH_{ICE}$  (relative humidity over ice) profiles in Figs. 3a and c at 10.5 km (28 October) and 11 km (30 October) indicates the tropopause. We show the volume depolarization ratio in Fig. 3b to better identify the smoke layers at 10-12 km and at 6 km height on this day. The white, tilted column-like features in Figs. 3b and d are ice virga consisting of falling ice crystals. The nucleation of ice crystals on smoke particles most probably started at the top of the humid layer in the coldest part of the troposphere (at temperatures from  $-47$  to  $-53^{\circ}\text{C}$ ). These ice crystals grew fast in the supersaturated air and immediately started to fall. Well-structured coherent virga are formed by these crystals. The hexagonal ice crystals cause strong depolarization ratios around 40%. The virga are visible as long as the  $RH_{ICE}$  is high so that sublimation of ice crystals, even in subsaturated air, is slow or prohibited.

Cirrus formation intensified on 30 October from 6 UTC to 12 UTC and the optical depth of the virga increased so that the smoke layer above the virga was no longer visible in Fig. 3d (after 9:45 UTC). The color plot is based on lidar profiles measured with 7.5 m vertical and 30 s temporal resolution. Averaging of signal profiles over, e.g., 15-20 minutes and vertical

smoothing with window lengths of 150-750 m is required to resolve the full cirrus and smoke layer structures up to the smoke layer top.

250 An intensification of ice virga backscattering was then observed over many hours in the evening of 30 October 2020 implying that strong ice nucleation by the smoke particles occurred at temperatures around  $-50^{\circ}\text{C}$  (Fig. 4). The top height of the virga zone always coincided with the lower part of the smoke layer. By using the classical Raman lidar technique (Ansmann et al., 1992; Wandinger, 1998) we analyzed the cirrus virga on 30 October 2020 in detail. The multiple-scattering-corrected 532 nm extinction coefficient  $\sigma_{532}$  of the ice crystals reached values as high as  $400 \text{ Mm}^{-1}$  (10:00-10:30 UTC mean values for the  
255 8-11 km height range in Fig. 3d),  $180 \text{ Mm}^{-1}$  (19:40-21:20 UTC, 8-10 km height range in Fig. 4), and  $1000 \text{ Mm}^{-1}$  (23:40-24:00 UTC, 8-10 km height range in Fig. 4). The respective cirrus optical depths were 0.8 (10:00-10:30 UTC), 0.25-0.3 (19:40-21.20 UTC), and 1.8-2.0 (23:40-24:00 UTC).

The pronounced virga structures point to a relatively small number of comparably large ice crystals that grew fast and formed these well-organized virga signatures. A broad crystal size spectrum (causing a respectively broad spectrum of sedimentation  
260 velocities) would probably not be able to produce such coherent virga structures over many hours. Patchy and incoherent cirrus structures would be more likely. We estimated the ice crystal number concentration  $n_{\text{ICE}}$  by using the relationship  $\sigma_{532} \approx n_{\text{ICE}} 2\pi r_{\text{eff}}^2$  (Schumann et al., 2011) with the measured 532 nm extinction coefficient  $\sigma_{532}$  and values for the assumed effective crystal radius  $r_{\text{eff}}$ . For  $\sigma_{532} = 400 \text{ Mm}^{-1}$  (as observed on 30 October, 10:00-10:30 UTC), we yield  $n_{\text{ICE}} = 100 \text{ L}^{-1}$  ( $r_{\text{eff}} = 25 \mu\text{m}$ ),  $50 \text{ L}^{-1}$  ( $r_{\text{eff}} = 35 \mu\text{m}$ ),  $25 \text{ L}^{-1}$  ( $r_{\text{eff}} = 50 \mu\text{m}$ ), and  $6 \text{ L}^{-1}$  ( $r_{\text{eff}} = 100 \mu\text{m}$ ). According to satellite observations  
265 over East Asia (15-55°N, 70-135°E, 2007-2015), analyzed by Zhao et al. (2018), typical values of the ice crystal  $r_{\text{eff}}$  are 25-35  $\mu\text{m}$ . For typical cirrus extinction coefficients of 100-200  $\text{Mm}^{-1}$ ,  $n_{\text{ICE}}$  values are thus in the range of 10-50  $\text{L}^{-1}$  according to our rough estimations here.

Figures 5 and 6 provide a more detailed, quantitative insight into the impact of the Californian wildfire smoke on ice nucleation over the Eastern Mediterranean. The lidar observations in Figs. 5 and 6 show the aerosol conditions before first ice  
270 clouds and virga developed on these two days. As can be seen, the smoke layer sufficiently overlapped with the humid region in the uppermost troposphere and thus was able to influence the development of cirrus clouds and virga significantly. In Fig. 5, we used both methods (Klett-Fernald approach, Raman lidar approach, see Sect. 2.2) to compute smoke backscatter profiles. Then, we multiplied the backscatter coefficients with the smoke lidar ratio of 75 sr to obtain the respective particle extinction coefficients for several cirrus-free time periods on 28 and 30 October 2020. Very polluted conditions prevailed. High particle  
275 extinction coefficients of up to  $250 \text{ Mm}^{-1}$  (28 October) and  $150 \text{ Mm}^{-1}$  (30 October) were observed. The aerosol optical thickness (AOT, 532 nm) of the smoke layer (8-12.5 km height range) was close to 0.2 on 28 October and about 0.16 on 30 October (9.5-12.5 km height range). Good agreement with the early morning AERONET photometer observations at Limassol, Cyprus, of the total 500 nm AOT was found (AERONET, 2023). Besides the smoke, dust and urban haze (below 5 km height in Fig. 3) contributed by about 0.05-0.1 to the overall 500 nm AOT of 0.25-0.3 (shortly after sunset on 28 October 2020) and  
280 from 0.22-0.25 (shortly after sunset on 30 October 2020).

In Fig. 6, particle surface area concentrations (PSAC) are presented, obtained by conversion of the extinction coefficients in Fig. 5 into surface area values by means of Eq. (1) in Sect. 3. In terms of PSAC, we see a clear overlap between the height

range with smoke traces and the ice nucleation height region. The smoke PSAC values (required in the INP estimation with Eqs. (5) and (6), Sect. 3.1) were enhanced in the humid layer down to about 9.4 km on 28 October and 8.5 km on 30 October. The smoke PSAC values were around  $25 \mu\text{m}^2 \text{cm}^{-3}$  at 10.4 km height on the two days (28 and 30 October) and even close to  $100 \mu\text{m}^2 \text{cm}^{-3}$  at the tropopause at 11 km height on 30 October 2020. The pronounced  $\text{RH}_{\text{ICE}}$  variability in the uppermost part of the humid layer in Fig. 6 may indicate water vapor consumption during the ice nucleation and subsequent crystal growth processes.

Regarding the ice nucleation mode, we hypothesize that the smoke particles were glassy so that DIN dominated ice formation (Murray et al., 2010). As shown in Figs. 5 and 6, the maximum particle concentration was found above the tropopause. Below the tropopause, the aerosol reservoir was obviously already strongly depleted as a result of ice nucleation, scavenging of aerosol particles by ice crystals, especially during the phase of the fast diffusional growth of small ice crystals (Oraltay and Hallett, 1990; Santachiara et al., 2018), and crystal sedimentation processes.

The radiosonde observations frequently showed  $\text{RH}_{\text{ICE}}$  values of  $>110\%$  over extended vertical ranges in the upper part of the cirrus layers.  $\text{RH}_{\text{ICE}}$  reached values of 115-120% (partly 125%) in the height range from 9.75-10 km on 28 and 30 October 2020. In the case of ice-active dust and ash particles, able to initiate ice nucleation already at ice supersaturations  $S_{\text{ICE}} < 1.1$  one would expect ice saturation ( $S_{\text{ICE}}$  around 1.0) in the presence of growing ice crystals and virga. Equilibrium at ice supersaturation conditions is a sign for a low crystal number concentration ( $<35 \text{L}^{-1}$ ) (Murray et al., 2010). Such a low amount of ice crystals is not able to quench the supersaturation which is in turn indicative for heterogeneous ice nucleation. Homogeneous freezing (of liquid aerosol particles) would produce crystal concentrations of  $>500 \text{L}^{-1}$  so that equilibrium at  $S_{\text{ICE}}$  around 1.0 would occur within a short time period.

### 4.3 Ice nucleation triggered by gravity wave activity: observation and simulation

On 1 November 2020, several pronounced gravity waves (GWs) produced wave-like cirrus features in the smoke-polluted air (9.5-11 km height). This measurement is shown in Fig. 7. It is well known that, besides the aerosol and humidity conditions, the occurrence of GWs in the upper troposphere plays a crucial role in cirrus formation processes (Kim et al., 2016; Kärcher and Podglajen, 2019; Kärcher et al., 2022). During the updraft phase, the temperature  $T$  decreases and  $S_{\text{ICE}}$  increases in the lofted air parcels and ice nucleation starts when  $\text{RH}_{\text{ICE}}$  exceeds a certain threshold. Ubiquitous mesoscale GWs generate the high cooling rates and ice supersaturation conditions required to initiate ice nucleation.

The GWs on 1 November 2020 did not cross the lidar station directly. We only saw the impact of the GWs, propagating from east to west across the Mediterranean Sea south of Limassol, on cirrus formation. GWs propagate with typical horizontal (travel) velocities of  $15\text{-}20 \text{m s}^{-1}$  and show temporal lengths of 15-25 minutes (Kalesse and Kollias, 2013). The waves on 1 November traveled almost against the southwesterly air flow (wind direction of  $230^\circ$ , wind velocity of  $13 \text{m s}^{-1}$ ) according to the Nicosia radiosonde observations. The remaining wave-induced cirrus patterns drifted with the southwesterly winds across the lidar station. We saw the end of the wave-like cirrus features first (around 9:50 and around 11:30 UTC), and the front part of the wave-induced cirrus, i.e., the ice nucleation region, much later (around 10:30 UTC and 12:20 UTC). Strong cooling occurs during lofting and generates high ice supersaturations so that heterogeneous ice nucleation can start on the available

INPs. The apparent amplitude (measured with lidar when the cirrus features crossed the field site) was roughly 300-400 m on 1 November 2020 (see Fig. 7). If we take ice virga development into account, the true amplitude of the gravity wave may have been between 200-250 m. Ice crystals, falling out of a cirrus layer, may reach heights of 100-200 m below the main cirrus deck within 5-20 minutes and may thus not allow us to detect the true wave amplitude and the height range influenced by the gravity wave motions.

In support to the lidar observations on 1 November, we performed simulations of gravity-wave-induced lofting of air parcels, the related temperature decrease and respective RH increase, and the impact of this lofting on ice nucleation via DIN. The goal of the simplified simulations was just to show that 200-250 m of lofting is sufficient to activate 10-50 INPs per liter, and thus to produce INP number concentrations high enough to prevent homogeneous freezing. The atmospheric meteorological and aerosol conditions as measured with lidar and Nicosia radiosondes on 1 November 2020 in the upper troposphere were used as input. The height of 9920 m (in the center of the humid layer in Fig. 7a) was selected as starting height of the lofting process. Different wave amplitudes (or air parcel ascents) from 200-250 m were simulated. Calculation step width was  $\Delta t = 10$  s in Eq. (6) in Sect. 3.1. The water vapor mixing ratio in the air parcels remained constant during the lofting process, i.e., no turbulent mixing and exchange process between air parcels occurred.

The results are shown in Fig. 8. They suggest that the gravity wave amplitude was probably around 220-225 m. As shown in Fig. 8, the accumulated INP number concentrations increased to values of about 30 to 550  $\text{L}^{-1}$  after an ascent of 220-230 m (from 9920 m to 10140-10150 m). For larger wave amplitudes (240 and 250 m) the INP number concentrations reached unrealistically high values of about 800 to almost 10000  $\text{L}^{-1}$ . We assume that the ice nucleation process stops before the INP number concentration exceeds 50-100  $\text{L}^{-1}$  because of water vapor deposition on the freshly formed ice crystals and the corresponding significant reduction of  $S_{\text{ICE}}$  (Murray et al., 2010; Kärcher et al., 2022) so that further ice nucleation is suppressed.

We expanded the gravity-wave simulations and included the 28 and 30 October observations. An overview of the simulated atmospheric conditions during the gravity wave events on 28 October (GW1), 30 October (GW2), and 1 November 2020 (GW3) according to the Nicosia radiosonde observations are depicted in Fig. 9. In addition, the specific ice nucleation conditions in the case of organic aerosol particles are highlighted. The GW temperature and  $\text{RH}_{\text{ICE}}$  ranges for initial and full GW periods indicate that heterogeneous ice nucleation dominated.  $\text{RH}_{\text{ICE}}$  values, required for homogeneous ice nucleation, were never reached in the simulations so that heterogeneous ice nucleation could proceed without competition with homogeneous freezing processes. The environmental and ice nucleation conditions of the GW events mostly represent conditions where organic aerosol (OA) particles are solid in phase when comparing with glass transition temperatures ( $T_g$ ) of secondary organic aerosol (SOA) particles derived from  $\alpha$ -pinene and naphthalene precursor gases (Charnawskas et al., 2017), ambient SOA particles (Wang et al., 2012b), and fulvic acid particles (Wang et al., 2012b). It should be noted that even  $\alpha$ -pinene derived SOA with the lowest  $T_g$  does not fully deliquesce, assuming an updraft of  $1 \text{ m s}^{-1}$  (Charnawskas et al., 2017), until  $\text{RH}_{\text{ICE}}$  values close to and above the homogeneous freezing limit are reached. OA particles that contain molecular species with higher molecular weights, such as fulvic acid compounds, are expected to retain the solid phase to even greater  $\text{RH}_{\text{ICE}}$  values (Koop et al.,

2011). This supports the notion that smoke particles were likely solid and acted as heterogeneous INPs in the deposition ice nucleation processes.

The simulation results for 28 October are shown in Fig. 10. For comparison, we included the immersion freezing (ABIFM) simulations. The predicted ice crystal number concentration ICNC (open symbols, ICNC=INP number concentration) for each calculation  $\Delta t = 10$  s as well as integral or the sum of formed ice crystals (or INP number concentration, solid symbols) are plotted. The respective changes in ice supersaturation  $S_{ICE}$  and  $\Delta a_w$  (Eq. 3) are shown in Fig. 10b. Starting height of the simulation was at 10400 m in the uppermost part of the humid layer (Fig. 6). Updraft velocities were  $0.3\text{--}0.4\text{ m s}^{-1}$ . The required smoke PSAC input values were taken from the lidar observations (from Fig. 6).

As can be seen, 120 m lofting is sufficient to obtain ice crystal number concentrations of the order of  $100\text{ L}^{-1}$  via immersion freezing (ABIFM) and close to  $50\text{ L}^{-1}$  via DIN at temperatures around  $-50^\circ\text{C}$  and for the simulated PSAC values (Figs. 10a).  $S_{ICE}$  and  $\Delta a_w$  increase during lofting and threshold values of 1.35-1.36 and 0.22-0.24 must be exceeded before efficient ice nucleation is initiated by the smoke particles via ABIFM. In the case of DIN, a significant increase of the INP number concentration occurred for  $S_{ICE} > 1.38\text{--}1.4$ . To initiate homogeneous freezing,  $S_{ICE}$  values  $\geq 1.5$  are required at temperatures around  $-50^\circ\text{C}$ . Already heterogeneously nucleated and growing ice crystals, however, will quickly lead to a reduction of  $S_{ICE}$  so that  $S_{ICE} > 1.5$  may never be reached, even during very strong updrafts triggering strong cooling rates. Similar results are obtained in the simulation of the 30 October measurement (not shown here) with a starting height at 10850 m (located in the uppermost part of the humid layer in Fig. 6) and a wave amplitude of 190 m. Thus, lofting by about 100-200 m is sufficient to initiate significant heterogeneous ice nucleation.

It should be mentioned at the end that these simplified simulations are conducted to provide insight in the principle ability of smoke particles to initiate cirrus formation during the passage of a GW. They do not allow us to draw any conclusion on the further cirrus evolution. The latest status regarding comprehensive cirrus modeling with focus on the role of heterogeneous ice nucleation may be found in Kärcher et al. (2022). In the case of organic aerosol particles, sophisticated simulations need to include complex aerosol particle compositions and all the potential complex ice nucleation processes due to amorphous phase transitions of the various organic phases as discussed in Berkemeier et al. (2014); Zobrist et al. (2008); Knopf et al. (2018); Charnawskas et al. (2017); Wang et al. (2012b); Lienhard et al. (2015).

## 5 Conclusion/Outlook

Based on lidar observations at Limassol, Cyprus, in the Eastern Mediterranean we found clear evidence for the impact of wildfire smoke on cirrus formation in the tropopause region at  $-47$  to  $-53^\circ\text{C}$ . Optically dense smoke layers crossed the Mediterranean Basin in October-November 2020. Several observational cases of smoke-cirrus interaction have been discussed. Simplified gravity wave simulations were in line with the observations. Lofting by about 100-200 m was found to be sufficient to initiate significant ice nucleation on the wildfire particles which mainly contain organic material.

We will continue our research on the impact of wildfire smoke and cirrus evolution processes by analyzing lidar observations in the central Arctic in the framework of the MOSAiC expedition in 2019-2020. We observed more than 50 cirrus systems



which evolved in smoke-polluted air (Engelmann et al., 2021; Ansmann et al., 2023). The advantage of the MOSAiC campaign is that, in addition to the lidar-derived INP estimates, the ice crystal number concentration can be obtained from combined radar-lidar observations (Bühl et al., 2019) so that closure studies such as presented by Ansmann et al. (2019a) are possible. In this way, more quantitative conclusions regarding INP levels and nucleated ice crystal number concentrations can be drawn. A rigorous uncertainty analysis does often not provide a realistic picture of the true error margins in active remote sensing applications. Closure studies, conducted to find consistency in the overall result data sets (from observations, parameterizations, and simulations) is then the most promising way to increase the reliability of observational findings.

In this article, we used a specific INP parameterization, developed for organic aerosol particles, to describe the ice-nucleating efficiency of aged wildfire smoke particles. Future work must include airborne sampling of aged smoke particles (after long range transport over weeks to months), that would allow multi-modal micro-spectroscopic analysis and chemical imaging of these aged wildfire smoke particles (Laskin et al., 2016, 2019; Knopf et al., 2014, 2022; Lata et al., 2021) coupled to laboratory-based characterization of their ice nucleation properties.

## 6 Data availability

Polly lidar observations (level 0 data, measured signals) are in the PollyNet database (PollyNET, 2023). All the analysis products are available upon request (info@tropos.de). Radiosonde data (Nicosia-Athalassa2023) are available at <https://www.meteociel.fr/observations-meteo/sondage.php?map=1> (Nicosia-Athalassa-RS, 2023) in archiving form and in a daily basis at the WMO Information System Portal through the link <https://gisc.dwd.de/wisportal/>. Backward trajectory analysis has been performed by air mass transport computation with the NOAA (National Oceanic and Atmospheric Administration) HYSPLIT (HYbrid Single-Particle Lagrangian Integrated Trajectory) model (HYSPLIT, 2023). AERONET observational data are downloaded from the respective data base (AERONET, 2023).

## 7 Author contributions

The paper was written by REM and AA under strong support of DAK. The gravity wave model was developed by AA. The data analysis was performed by KO, REM, and HB. RE, AN, AS, PS, JB, and DE were involved in the setup of the instrumentation, calibration and quality tests, and maintenance of the station. UW and DH are involved in the project EXCELSIOR. All coauthors were actively involved in the extended discussions and the elaboration of the final design of the manuscript.

## 8 Competing interests

Daniel A. Knopf is a member of the editorial board of Atmospheric Chemistry and Physics.

## 9 Financial support

The authors acknowledge the ‘EXCELSIOR’: ERATOSTHENES: EXcellence research Centre for Earth Surveillance and Space-Based Monitoring of the Environment H2020 Widespread Teaming project ([www.excelsior2020.eu](http://www.excelsior2020.eu)). The ‘EXCELSIOR’ project has received funding from the European Union’s Horizon 2020 research and innovation programme under Grant Agreement No 857510, from the Government of the Republic of Cyprus through the Directorate General for the European Programmes, Coordination and Development and the Cyprus University of Technology. The authors acknowledge support through the European Research Infrastructure for the observation of Aerosol, Clouds and Trace Gases ACTRIS under grant agreement no. 654109 and 739530 from the European Union’s Horizon 2020 research and innovation programme. The PollyXT-CYP was funded by the German Federal Ministry of Education and Research (BMBF) via the PoLiCyTa project (grant no. 01LK1603A).

415 The study is supported by “ACCEPT” project (Prot. No: LOCALDEV-0008) co-financed by the Financial Mechanism of Norway (85%) and the Republic of Cyprus (15%) in the framework of the programming period 2014 - 2021. The lidar analysis on smoke-cirrus interaction was further supported by BMBF funding of the SCiAMO project (MOSAIC-FKZ 03F0915A). DAK acknowledges support by U.S. Department of Energy’s (DOE) Atmospheric System Research (ASR) program, Office of Biological and Environmental Research (OBER) (grant no. DE-SC0021034).

420

425 *Acknowledgements.* We are very grateful to Nicosia-Athalassa radiosonde station for excellent radiosonde observations and especially to Demetris Charalambous, Meteorology Officer at the Cyprus Department of Meteorology, for the provision of historic data. We also thank the HYSPLIT team for an easy-to-use internet platform.

## References

- Abatzoglou, J. T., Williams, A. P., and Barbero, R.: Global emergence of anthropogenic climate change in fire weather indices, *Geophys. Res. Lett.*, 46, 326–336, <https://doi.org/10.1029/2018GL080959>, 2019.
- ACTRIS(2023): Aerosols, Clouds and Trace gases Research InfraStructure home page, available at: <https://www.actris.eu/>, last access: 27 March, 2023.
- AERONET(2023): Aerosol Robotic Network aerosol data base, available at: <http://aeronet.gsfc.nasa.gov/>, last access: 27 March, 2023.
- Ansmann, A., Wandinger, U., Riebesell, M., Weitkamp, C., and Michaelis, W.: Independent measurement of extinction and backscatter profiles in cirrus clouds by using a combined Raman elastic-backscatter lidar, *Appl. Opt.*, 31, 7113–7131, <https://doi.org/10.1364/AO.31.007113>, 1992.
- Ansmann, A., Mamouri, R.-E., Bühl, J., Seifert, P., Engelmann, R., Hofer, J., Nisantzi, A., Atkinson, J. D., Kanji, Z. A., Sierau, B., Vrekoussis, M., and Sciare, J.: Ice-nucleating particle versus ice crystal number concentration in altocumulus and cirrus layers embedded in Saharan dust: a closure study, *Atmospheric Chemistry and Physics*, 19, 15 087–15 115, <https://doi.org/10.5194/acp-19-15087-2019>, 2019a.
- Ansmann, A., Mamouri, R.-E., Hofer, J., Baars, H., Althausen, D., and Abdullaev, S. F.: Dust mass, cloud condensation nuclei, and ice-nucleating particle profiling with polarization lidar: updated POLIPHON conversion factors from global AERONET analysis, *Atmospheric Measurement Techniques*, 12, 4849–4865, <https://doi.org/10.5194/amt-12-4849-2019>, 2019b.
- Ansmann, A., Ohneiser, K., Mamouri, R.-E., Knopf, D. A., Veselovskii, I., Baars, H., Engelmann, R., Foth, A., Jimenez, C., Seifert, P., and Barja, B.: Tropospheric and stratospheric wildfire smoke profiling with lidar: mass, surface area, CCN, and INP retrieval, *Atmospheric Chemistry and Physics*, 21, <https://doi.org/10.5194/acp-21-9779-2021>, 2021.
- Ansmann, A., Ohneiser, K., Engelmann, R., Radenz, M., Griesche, H., Hofer, J., Althausen, D., Creamean, J. M., Boyer, M. C., Knopf, D. A., Dahlke, S., Maturilli, M., Gebauer, H., Bühl, J., Jimenez, C., Seifert, P., and Wandinger, U.: Annual cycle of aerosol properties over the central Arctic during MOSAiC 2019–2020 — light-extinction, CCN, and INP levels from the boundary layer to the tropopause, *EGUsphere*, 2023, 1–44, <https://doi.org/10.5194/egusphere-2023-444>, 2023.
- Baars, H., Kanitz, T., Engelmann, R., Althausen, D., Heese, B., Komppula, M., Preißler, J., Tesche, M., Ansmann, A., Wandinger, U., Lim, J.-H., Ahn, J. Y., Stachlewska, I. S., Amiridis, V., Marinou, E., Seifert, P., Hofer, J., Skupin, A., Schneider, F., Bohlmann, S., Foth, A., Bley, S., Pfüller, A., Giannakaki, E., Lihavainen, H., Viisanen, Y., Hooda, R. K., Pereira, S. N., Bortoli, D., Wagner, F., Mattis, I., Janicka, L., Markowicz, K. M., Achtert, P., Artaxo, P., Pauliquevis, T., Souza, R. A. F., Sharma, V. P., van Zyl, P. G., Beukes, J. P., Sun, J., Rohwer, E. G., Deng, R., Mamouri, R.-E., and Zamorano, F.: An overview of the first decade of Polly<sup>NET</sup>: an emerging network of automated Raman-polarization lidars for continuous aerosol profiling, *Atmospheric Chemistry and Physics*, 16, 5111–5137, <https://doi.org/10.5194/acp-16-5111-2016>, 2016.
- Baars, H., Ansmann, A., Ohneiser, K., Haarig, M., Engelmann, R., Althausen, D., Hanssen, I., Gausa, M., Pietruczuk, A., Szkop, A., Stachlewska, I. S., Wang, D., Reichardt, J., Skupin, A., Mattis, I., Trickl, T., Vogelmann, H., Navas-Guzmán, F., Haeefe, A., Acheson, K., Ruth, A. A., Tatarov, B., Müller, D., Hu, Q., Podvin, T., Goloub, P., Veselovskii, I., Pietras, C., Haeffelin, M., Fréville, P., Sicard, M., Comerón, A., Fernández García, A. J., Molero Menéndez, F., Córdoba-Jabonero, C., Guerrero-Rascado, J. L., Alados-Arboledas, L., Bortoli, D., Costa, M. J., Dionisi, D., Liberti, G. L., Wang, X., Sannino, A., Papagiannopoulos, N., Boselli, A., Mona, L., D’Amico, G., Romano, S., Perrone, M. R., Belegante, L., Nicolae, D., Grigorov, I., Gialitaki, A., Amiridis, V., Soupiona, O., Papayannis, A., Mamouri, R.-E., Nisantzi, A., Heese, B., Hofer, J., Schechner, Y. Y., Wandinger, U., and Pappalardo, G.: The unprecedented 2017–2018 stratospheric

465 smoke event: decay phase and aerosol properties observed with the EARLINET, *Atmospheric Chemistry and Physics*, 19, 15 183–15 198, <https://doi.org/10.5194/acp-19-15183-2019>, 2019.

Baars, H., Radenz, M., Floutsi, A. A., Engelmann, R., Althausen, D., Heese, B., Ansmann, A., Flament, T., Dabas, A., Tracon, D., Reitebuch, O., Bley, S., and Wandinger, U.: Californian wildfire smoke over Europe: A first example of the aerosol observing capabilities of Aeolus compared to ground-based lidar, 48, <https://doi.org/10.1029/2020GL092194>, <http://resolver.sub.uni-goettingen.de/purl?gldocs-11858/8745>, 2021.

470 Barry, K. R., Hill, T. C. J., Levin, E. J. T., Twohy, C. H., Moore, K. A., Weller, Z. D., Toohey, D. W., Reeves, M., Campos, T., Geiss, R., Schill, G. P., Fischer, E. V., Kreidenweis, S. M., and DeMott, P. J.: Observations of Ice Nucleating Particles in the Free Troposphere From Western US Wildfires, *Journal of Geophysical Research: Atmospheres*, 126, e2020JD033 752, <https://doi.org/10.1029/2020JD033752>, e2020JD033752 2020JD033752, 2021.

475 Berkemeier, T., Shiraiwa, M., Pöschl, U., and Koop, T.: Competition between water uptake and ice nucleation by glassy organic aerosol particles, *Atmospheric Chemistry and Physics*, 14, 12 513–12 531, <https://doi.org/10.5194/acp-14-12513-2014>, 2014.

Bühl, J., Seifert, P., Radenz, M., Baars, H., and Ansmann, A.: Ice crystal number concentration from lidar, cloud radar and radar wind profiler measurements, *Atmospheric Measurement Techniques*, 12, 6601–6617, <https://doi.org/10.5194/amt-12-6601-2019>, 2019.

Burton, S. P., Hair, J. W., Kahnert, M., Ferrare, R. A., Hostetler, C. A., Cook, A. L., Harper, D. B., Berkoff, T. A., Seaman, S. T., Collins, J. E., 480 Fenn, M. A., and Rogers, R. R.: Observations of the spectral dependence of linear particle depolarization ratio of aerosols using NASA Langley airborne High Spectral Resolution Lidar, *Atmospheric Chemistry and Physics*, 15, 13 453–13 473, <https://doi.org/10.5194/acp-15-13453-2015>, 2015.

Charnawskas, J. C., Alpert, P. A., Lambe, A. T., Berkemeier, T., O’Brien, R. E., Massoli, P., Onasch, T. B., Shiraiwa, M., Moffet, R. C., Gilles, M. K., Davidovits, P., Worsnop, D. R., and Knopf, D. A.: Condensed-phase biogenic–anthropogenic interactions with implications 485 for cold cloud formation, *Faraday Discuss.*, 200, 165–194, <https://doi.org/10.1039/C7FD00010C>, 2017.

Chou, C., Kanji, Z. A., Stetzer, O., Tritscher, T., Chirico, R., Heringa, M. F., Weingartner, E., Prévôt, A. S. H., Baltensperger, U., and Lohmann, U.: Effect of photochemical ageing on the ice nucleation properties of diesel and wood burning particles, *Atmospheric Chemistry and Physics*, 13, 761–772, <https://doi.org/10.5194/acp-13-761-2013>, 2013.

Dahlkötter, F., Gysel, M., Sauer, D., Minikin, A., Baumann, R., Seifert, P., Ansmann, A., Fromm, M., Voigt, C., and Weinzierl, B.: The 490 Pagami Creek smoke plume after long-range transport to the upper troposphere over Europe - aerosol properties and black carbon mixing state, *Atmospheric Chemistry and Physics*, 14, 6111–6137, <https://doi.org/10.5194/acp-14-6111-2014>, 2014.

DeMott, P. J., Prenni, A. J., McMeeking, G. R., Sullivan, R. C., Petters, M. D., Tobo, Y., Niemand, M., Möhler, O., Snider, J. R., Wang, Z., and Kreidenweis, S. M.: Integrating laboratory and field data to quantify the immersion freezing ice nucleation activity of mineral dust particles, *Atmospheric Chemistry and Physics*, 15, 393–409, <https://doi.org/10.5194/acp-15-393-2015>, 2015.

495 Engelmann, R., Kanitz, T., Baars, H., Heese, B., Althausen, D., Skupin, A., Wandinger, U., Komppula, M., Stachlewska, I. S., Amiridis, V., Marinou, E., Mattis, I., Linné, H., and Ansmann, A.: The automated multiwavelength Raman polarization and water-vapor lidar Polly<sup>XT</sup>: the neXT generation, *Atmospheric Measurement Techniques*, 9, 1767–1784, <https://doi.org/10.5194/amt-9-1767-2016>, 2016.

Engelmann, R., Ansmann, A., Ohneiser, K., Griesche, H., Radenz, M., Hofer, J., Althausen, D., Dahlke, S., Maturilli, M., Veselovskii, I., Jimenez, C., Wiesen, R., Baars, H., Bühl, J., Gebauer, H., Haarig, M., Seifert, P., Wandinger, U., and Macke, A.: Wildfire smoke, Arctic 500 haze, and aerosol effects on mixed-phase and cirrus clouds over the North Pole region during MOSAiC: an introduction, *Atmospheric Chemistry and Physics*, 21, <https://doi.org/10.5194/acp-21-13397-2021>, 2021.

- Fernald, F. G.: Analysis of atmospheric lidar observations: some comments, *Appl. Opt.*, 23, 652–653, <https://doi.org/10.1364/AO.23.000652>, 1984.
- Floutsi, A. A., Baars, H., Radenz, M., Haarig, M., Yin, Z., Seifert, P., Jimenez, C., Ansmann, A., Engelmann, R., Barja, B., Zamorano, F.,  
505 and Wandinger, U.: Advection of Biomass Burning Aerosols towards the Southern Hemispheric Mid-Latitude Station of Punta Arenas as Observed with Multiwavelength Polarization Raman Lidar, *Remote Sens.*, 13, <https://doi.org/10.3390/rs13010138>, 2021.
- Foth, A., Kanitz, T., Engelmann, R., Baars, H., Radenz, M., Seifert, P., Barja, B., Fromm, M., Kalesse, H., and Ansmann, A.: Vertical aerosol distribution in the southern hemispheric midlatitudes as observed with lidar in Punta Arenas, Chile (53.2° S and 70.9° W), during ALPACA, *Atmospheric Chemistry and Physics*, 19, 6217–6233, <https://doi.org/10.5194/acp-19-6217-2019>, 2019.
- 510 Froyd, K. D., Murphy, D. M., Lawson, P., Baumgardner, D., and Herman, R. L.: Aerosols that form subvisible cirrus at the tropical tropopause, *Atmospheric Chemistry and Physics*, 10, 209–218, <https://doi.org/10.5194/acp-10-209-2010>, 2010.
- Froyd, K. D., Yu, P., Schill, G. P., Brock, C. A., Kupc, A., Williamson, C. J., Jensen, E. J., Ray, E., Rosenlof, K. H., Bian, H., Darmenov, A. S., Colarco, P. R., Diskin, G. S., Bui, T., and Murphy, D. M.: Dominant role of mineral dust in cirrus cloud formation revealed by global-scale measurements, *Nature Geoscience*, 15, 177–183, <https://doi.org/10.1038/s41561-022-00901-w>, 2022.
- 515 Gialitaki, A., Tsekeri, A., Amiridis, V., Ceolato, R., Paulien, L., Kampouri, A., Gkikas, A., Solomos, S., Marinou, E., Haarig, M., Baars, H., Ansmann, A., Lapyonok, T., Lopatin, A., Dubovik, O., Groß, S., Wirth, M., Tsichla, M., Tsikoudi, I., and Balis, D.: Is the near-spherical shape the “new black” for smoke?, *Atmospheric Chemistry and Physics*, 20, 14 005–14 021, <https://doi.org/10.5194/acp-20-14005-2020>, 2020.
- Haarig, M., Ansmann, A., Baars, H., Jimenez, C., Veselovskii, I., Engelmann, R., and Althausen, D.: Depolarization and lidar ratios at 355,  
520 532, and 1064 nm and microphysical properties of aged tropospheric and stratospheric Canadian wildfire smoke, *Atmospheric Chemistry and Physics*, 18, 11 847–11 861, <https://doi.org/10.5194/acp-18-11847-2018>, 2018.
- Heymsfield, A. J. and Miloshevich, L. M.: Relative Humidity and Temperature Influences on Cirrus Formation and Evolution: Observations from Wave Clouds and FIRE II, *Journal of Atmospheric Sciences*, 52, 4302 – 4326, [https://doi.org/10.1175/1520-0469\(1995\)052<4302:RHATIO>2.0.CO;2](https://doi.org/10.1175/1520-0469(1995)052<4302:RHATIO>2.0.CO;2), 1995.
- 525 Hodzic, A., Campuzano-Jost, P., Bian, H., Chin, M., Colarco, P. R., Day, D. A., Froyd, K. D., Heinold, B., Jo, D. S., Katich, J. M., Kodros, J. K., Nault, B. A., Pierce, J. R., Ray, E., Schacht, J., Schill, G. P., Schroder, J. C., Schwarz, J. P., Sueper, D. T., Tegen, I., Tilmes, S., Tsigaridis, K., Yu, P., and Jimenez, J. L.: Characterization of organic aerosol across the global remote troposphere: a comparison of ATom measurements and global chemistry models, *Atmospheric Chemistry and Physics*, 20, 4607–4635, <https://doi.org/10.5194/acp-20-4607-2020>, 2020.
- 530 Hofer, J., Althausen, D., Abdullaev, S. F., Makhmudov, A. N., Nazarov, B. I., Schettler, G., Engelmann, R., Baars, H., Fomba, K. W., Müller, K., Heinold, B., Kandler, K., and Ansmann, A.: Long-term profiling of mineral dust and pollution aerosol with multiwavelength polarization Raman lidar at the Central Asian site of Dushanbe, Tajikistan: case studies, *Atmospheric Chemistry and Physics*, 17, 14 559–14 577, <https://doi.org/10.5194/acp-17-14559-2017>, 2017.
- Holben, B. N., Eck, T. F., Slutsker, I., Tanré, D., Buis, J. P., Setzer, A., Vermote, E., Reagan, J. A., Kaufman, Y. J., Nakajima, T., Lavenu,  
535 F., Jankowiak, I., and Smirnov, A.: AERONET - A federated instrument network and data archive for aerosol characterization, *Remote Sensing of Environment*, 66, 1–16, [https://doi.org/10.1016/S0034-4257\(98\)00031-5](https://doi.org/10.1016/S0034-4257(98)00031-5), 1998.
- Hu, Q., Goloub, P., Veselovskii, I., and Podvin, T.: The characterization of long-range transported North American biomass burning plumes: what can a multi-wavelength Mie–Raman-polarization-fluorescence lidar provide?, *Atmospheric Chemistry and Physics*, 22, 5399–5414, <https://doi.org/10.5194/acp-22-5399-2022>, 2022.

- 540 HYSPLIT(2023): HYbrid Single-Particle Lagrangian Integrated Trajectory model, backward trajectory calculation tool, available at: [http://ready.arl.noaa.gov/HYSPLIT\\_traj.php](http://ready.arl.noaa.gov/HYSPLIT_traj.php), last access: 27 March, 2023.
- Jahl, L. G., Brubaker, T. A., Polen, M. J., Jahn, L. G., Cain, K. P., Bowers, B. B., Fahy, W. D., Graves, S., and Sullivan, R. C.: Atmospheric aging enhances the ice nucleation ability of biomass-burning aerosol, *Sci. Adv.*, 7, <https://doi.org/10.1126/sciadv.abd3440>, 2021.
- Jahn, L. G., Polen, M. J., Jahl, L. G., Brubaker, T. A., Somers, J., and Sullivan, R. C.: Biomass combustion produces ice-active minerals in  
545 biomass-burning aerosol and bottom ash, *Proc. Natl. Acad. Sci. U.S.A.*, 117, 21 928–21 937, <https://doi.org/10.1073/pnas.1922128117>, 2020.
- Jimenez, C., Ansmann, A., Engelmann, R., Donovan, D., Malinka, A., Seifert, P., Wiesen, R., Radenz, M., Yin, Z., Bühl, J., Schmidt, J., Barja, B., and Wandinger, U.: The dual-field-of-view polarization lidar technique: a new concept in monitoring aerosol effects in liquid-water clouds – case studies, *Atmospheric Chemistry and Physics*, 20, 15 265–15 284, <https://doi.org/10.5194/acp-20-15265-2020>, 2020.
- 550 Jolly, W. M., Cochrane, M. A., Freeborn, P. H., Holden, Z. A., Brown, T. J., Williamson, G. J., and Bowman, D. M. J. S.: Climate-induced variations in global wildfire danger from 1979 to 2013, *Nature Communications*, 6, <https://doi.org/10.1038/ncomms8537>, 2015.
- Kalesse, H. and Kollias, P.: Climatology of high cloud dynamics using profiling ARM Doppler radar observations, *Journal of Climate*, 26, 6340–6359, <https://doi.org/10.1175/JCLI-D-12-00695.1>, 2013.
- Kanji, Z. A., Ladino, L. A., Wex, H., Boose, Y., Burkert-Kohn, M., Cziczo, D. J., and Krämer, M.: Overview of ice nucleating particles,  
555 Meteorological monographs, 58, 1 – 33, <https://doi.org/10.1175/AMSMONOGRAPHS-D-16-0006.1>, 2017.
- Kilchhofer, K., Mahrt, F., and Kanji, Z. A.: The Role of Cloud Processing for the Ice Nucleating Ability of Organic Aerosol and Coal Fly Ash Particles, *Journal of Geophysical Research: Atmospheres*, 126, e2020JD033 338, <https://doi.org/10.1029/2020JD033338>, e2020JD033338 2020JD033338, 2021.
- Kim, J.-E., Alexander, M. J., Bui, T. P., Dean-Day, J. M., Lawson, R. P., Woods, S., Hlavka, D., Pfister, L., and Jensen, E. J.: Ubiquitous  
560 influence of waves on tropical high cirrus clouds, *Geophysical Research Letters*, 43, 5895–5901, <https://doi.org/10.1002/2016GL069293>, 2016.
- Kirchmeier-Young, M. C., Gillett, N. P., Zwiers, F. W., Cannon, A. J., and Anslow, F. S.: Attribution of the influence of human- induced climate change on an extreme fire season, *Earths Future*, 7, 2–10, <https://doi.org/10.1029/2018EF001050>, 2019.
- Klett, J. D.: Stable analytic inversion solution for processing lidar returns, *Appl. Opt.*, 20, 211–220, <https://doi.org/10.1364/AO.20.000211>,  
565 1981.
- Kloss, C., Berthet, G., Sellitto, P., Ploeger, F., Bucci, S., Khaykin, S., Jégou, F., Taha, G., Thomason, L. W., Barret, B., Le Flochmoen, E., von Hobe, M., Bossolasco, A., Bègue, N., and Legras, B.: Transport of the 2017 Canadian wildfire plume to the tropics via the Asian monsoon circulation, *Atmospheric Chemistry and Physics*, 19, 13 547–13 567, <https://doi.org/10.5194/acp-19-13547-2019>, 2019.
- Knopf, D. A. and Alpert, P. A.: A water activity based model of heterogeneous ice nucleation kinetics for freezing of water and aqueous  
570 solution droplets, *Farad. Discuss.*, 165, 513–534, <https://doi.org/10.1039/c3fd00035d>, 2013.
- Knopf, D. A. and Alpert, P. A.: Atmospheric ice nucleation, *Nature Reviews Physics*, 5, 203–217, <https://doi.org/10.1038/s42254-023-00570-7>, 2023.
- Knopf, D. A., Alpert, P. A., Wang, B., O'Brien, R. E., Kelly, S. T., Laskin, A., Gilles, M. K., and Moffet, R. C.: Microspectroscopic imaging and characterization of individually identified ice nucleating particles from a case field study, *Journal of Geophysical Research: Atmospheres*, 119, 10,365–10,381, <https://doi.org/10.1002/2014JD021866>, 2014.
- 575 Knopf, D. A., Alpert, P. A., and Wang, B.: The role of organic aerosol in atmospheric ice nucleation: a review, *ACS Earth and Space Chemistry*, 2, 168–202, <https://doi.org/10.1021/acsearthspacechem.7b00120>, 2018.

Knopf, D. A., Charnawskas, J. C., Wang, P., Wong, B., Tomlin, J. M., Jankowski, K. A., Fraund, M., Veghte, D. P., China, S., Laskin, A.,  
 580 Moffet, R. C., Gilles, M. K., Aller, J. Y., Marcus, M. A., Raveh-Rubin, S., and Wang, J.: Micro-spectroscopic and freezing characterization  
 of ice-nucleating particles collected in the marine boundary layer in the eastern North Atlantic, *Atmospheric Chemistry and Physics*, 22,  
 5377–5398, <https://doi.org/10.5194/acp-22-5377-2022>, 2022.

Koop, T.: Homogeneous Ice Nucleation in Water and Aqueous Solutions, *Zeitschrift für Physikalische Chemie*, 218, 1231–1258,  
<https://doi.org/10.1524/zpch.218.11.1231.50812>, 2004.

Koop, T., Luo, B. P., Tsias, A., and Peter, T.: Water activity as the determinant for homogeneous ice nucleation in aqueous solutions, *Nature*,  
 585 406, 611–614, <https://doi.org/10.1038/35020537>, 2000.

Koop, T., Bookhold, J., Shiraiwa, M., and Pöschl, U.: Glass transition and phase state of organic compounds: dependency on molec-  
 ular properties and implications for secondary organic aerosols in the atmosphere, *Phys. Chem. Chem. Phys.*, 13, 19 238–19 255,  
<https://doi.org/10.1039/C1CP22617G>, 2011.

Kärcher, B. and Podglajen, A.: A Stochastic Representation of Temperature Fluctuations Induced by Mesoscale Gravity Waves, *Journal of*  
 590 *Geophysical Research: Atmospheres*, 124, 11 506–11 529, <https://doi.org/10.1029/2019JD030680>, 2019.

Kärcher, B., DeMott, P. J., Jensen, E. J., and Harrington, J. Y.: Studies on the Competition Between Homogeneous and  
 Heterogeneous Ice Nucleation in Cirrus Formation, *Journal of Geophysical Research: Atmospheres*, 127, e2021JD035 805,  
<https://doi.org/10.1029/2021JD035805>, e2021JD035805 2021JD035805, 2022.

Laskin, A., Gilles, M. K., Knopf, D. A., Wang, B., and China, S.: Progress in the Analysis of Complex Atmospheric Particles, *Annual Review*  
 595 *of Analytical Chemistry*, 9, 117–143, <https://doi.org/10.1146/annurev-anchem-071015-041521>, pMID: 27306308, 2016.

Laskin, A., Moffet, R. C., and Gilles, M. K.: Chemical Imaging of Atmospheric Particles, *Accounts of Chemical Research*, 52, 3419–3431,  
<https://doi.org/10.1021/acs.accounts.9b00396>, pMID: 31714061, 2019.

Lata, N. N., Zhang, B., Schum, S., Mazzoleni, L., Brimberry, R., Marcus, M. A., Cantrell, W. H., Fialho, P., Mazzoleni, C., and China, S.:  
 Aerosol Composition, Mixing State, and Phase State of Free Tropospheric Particles and Their Role in Ice Cloud Formation, *ACS Earth*  
 600 *and Space Chemistry*, 5, 3499–3510, <https://doi.org/10.1021/acsearthspacechem.1c00315>, 2021.

Lienhard, D. M., Huisman, A. J., Krieger, U. K., Rudich, Y., Marcolli, C., Luo, B. P., Bones, D. L., Reid, J. P., Lambe, A. T., Cana-  
 garatna, M. R., Davidovits, P., Onasch, T. B., Worsnop, D. R., Steimer, S. S., Koop, T., and Peter, T.: Viscous organic aerosol particles in  
 the upper troposphere: diffusivity-controlled water uptake and ice nucleation?, *Atmospheric Chemistry and Physics*, 15, 13 599–13 613,  
<https://doi.org/10.5194/acp-15-13599-2015>, 2015.

605 Mamouri, R.-E. and Ansmann, A.: Potential of polarization lidar to provide profiles of CCN- and INP-relevant aerosol parameters, *Atmo-  
 spheric Chemistry and Physics*, 16, 5905–5931, <https://doi.org/10.5194/acp-16-5905-2016>, 2016.

Mamouri, R.-E. and Ansmann, A.: Potential of polarization/Raman lidar to separate fine dust, coarse dust, maritime, and anthropogenic  
 aerosol profiles, *Atmospheric Measurement Techniques*, 10, 3403–3427, <https://doi.org/10.5194/amt-10-3403-2017>, 2017.

Mamouri, R. E., Ansmann, A., Nisantzi, A., Kokkalis, P., Schwarz, A., and Hadjimitsis, D.: Low Arabian dust extinction-to-backscatter ratio,  
 610 *Geophysical Research Letters*, 40, 4762–4766, <https://doi.org/10.1002/grl.50898>, 2013.

Mamouri, R.-E., Ansmann, A., Nisantzi, A., Solomos, S., Kallos, G., and Hadjimitsis, D. G.: Extreme dust storm over the eastern Mediter-  
 ranean in September 2015: satellite, lidar, and surface observations in the Cyprus region, *Atmospheric Chemistry and Physics*, 16, 13 711–  
 13 724, <https://doi.org/10.5194/acp-16-13711-2016>, 2016.

Marcolli, C.: Deposition nucleation viewed as homogeneous or immersion freezing in pores and cavities, *Atmospheric Chemistry and*  
 615 *Physics*, 14, 2071–2104, <https://doi.org/10.5194/acp-14-2071-2014>, 2014.

- Mardi, A. H., Dadashazar, H., MacDonald, A. B., Braun, R. A., Crosbie, E., Xian, P., Thorsen, T. J., Coggon, M. M., Fenn, M. A., Ferrare, R. A., Hair, J. W., Woods, R. K., Jonsson, H. H., Flagan, R. C., Seinfeld, J. H., and Sorooshian, A.: Biomass Burning Plumes in the Vicinity of the California Coast: Airborne Characterization of Physicochemical Properties, Heating Rates, and Spatiotemporal Features, *Journal of Geophysical Research: Atmospheres*, 123, 13,560–13,582, <https://doi.org/10.1029/2018JD029134>, 2018.
- 620 Marinou, E., Tesche, M., Nenes, A., Ansmann, A., Schrod, J., Mamali, D., Tsekeri, A., Pikridas, M., Baars, H., Engelmann, R., Voudouri, K.-A., Solomos, S., Sciare, J., Groß, S., Ewald, F., and Amiridis, V.: Retrieval of ice-nucleating particle concentrations from lidar observations and comparison with UAV in situ measurements, *Atmospheric Chemistry and Physics*, 19, 11 315–11 342, <https://doi.org/10.5194/acp-19-11315-2019>, 2019.
- Mattis, I., Müller, D., Ansmann, A., Wandinger, U., Preißler, J., Seifert, P., and Tesche, M.: Ten years of multiwavelength Raman lidar  
625 observations of free-tropospheric aerosol layers over central Europe: Geometrical properties and annual cycle, *Journal of Geophysical Research: Atmospheres*, 113, <https://doi.org/10.1029/2007JD009636>, 2008.
- Michailidis, K., Koukouli, M.-E., Balis, D., Veefkind, J. P., de Graaf, M., Mona, L., Papagianopoulos, N., Pappalardo, G., Tsikoudi, I., Amiridis, V., Marinou, E., Gialitaki, A., Mamouri, R.-E., Nisantzi, A., Bortoli, D., João Costa, M., Salgueiro, V., Papayannis, A., Mylonaki, M., Alados-Arboledas, L., Romano, S., Perrone, M. R., and Baars, H.: Validation of the TROPOMI/S5P aerosol layer height using  
630 EARLINET lidars, *Atmospheric Chemistry and Physics*, 23, 1919–1940, <https://doi.org/10.5194/acp-23-1919-2023>, 2023.
- Murray, B. J., Wilson, T. W., Dobbie, S., and Cui, Z.: Heterogeneous nucleation of ice particles on glassy aerosols under cirrus conditions, *Nature Geoscience*, 3, 233–237, <https://doi.org/10.1038/ngeo817>, 2010.
- Nicosia-Athalassa-RS(2023): Athalassa Radiosonde Station, Cyprus, profile data available at: <https://www.meteociel.fr/observations-meteo/sondage.php?map=1>, last access: 23 March, 2023.
- 635 Nisantzi, A., Mamouri, R. E., Ansmann, A., and Hadjimitsis, D.: Injection of mineral dust into the free troposphere during fire events observed with polarization lidar at Limassol, Cyprus, *Atmospheric Chemistry and Physics*, 14, 12 155–12 165, <https://doi.org/10.5194/acp-14-12155-2014>, 2014.
- Nisantzi, A., Mamouri, R. E., Ansmann, A., Schuster, G. L., and Hadjimitsis, D. G.: Middle East versus Saharan dust extinction-to-backscatter ratios, *Atmospheric Chemistry and Physics*, 15, 7071–7084, <https://doi.org/10.5194/acp-15-7071-2015>, 2015.
- 640 Ohneiser, K., Ansmann, A., Baars, H., Seifert, P., Barja, B., Jimenez, C., Radenz, M., Teisseire, A., Floutsi, A., Haarig, M., Foth, A., Chudnovsky, A., Engelmann, R., Zamorano, F., Bühl, J., and Wandinger, U.: Smoke of extreme Australian bushfires observed in the stratosphere over Punta Arenas, Chile, in January 2020: optical thickness, lidar ratios, and depolarization ratios at 355 and 532 nm, *Atmospheric Chemistry and Physics*, 20, 8003–8015, <https://doi.org/10.5194/acp-20-8003-2020>, 2020.
- Ohneiser, K., Ansmann, A., Chudnovsky, A., Engelmann, R., Ritter, C., Veselovskii, I., Baars, H., Gebauer, H., Griesche, H., Radenz, M.,  
645 Hofer, J., Althausen, D., Dahlke, S., and Maturilli, M.: The unexpected smoke layer in the High Arctic winter stratosphere during MOSAiC 2019–2020, *Atmospheric Chemistry and Physics*, 21, 15 783–15 808, <https://doi.org/10.5194/acp-21-15783-2021>, 2021.
- Ohneiser, K., Ansmann, A., Kaifler, B., Chudnovsky, A., Barja, B., Knopf, D. A., Kaifler, N., Baars, H., Seifert, P., Villanueva, D., Jimenez, C., Radenz, M., Engelmann, R., Veselovskii, I., and Zamorano, F.: Australian wildfire smoke in the stratosphere: the decay phase in  
2020/2021 and impact on ozone depletion, *Atmospheric Chemistry and Physics*, 22, 7417–7442, <https://doi.org/10.5194/acp-22-7417-2022>, 2022.  
650
- Ohneiser, K., Ansmann, A., Witthuhn, J., Deneke, H., Chudnovsky, A., Walter, G., and Senf, F.: Self-lofting of wildfire smoke in the troposphere and stratosphere: simulations and space lidar observations, *Atmospheric Chemistry and Physics*, 23, 2901–2925, <https://doi.org/10.5194/acp-23-2901-2023>, 2023.



- Oraltay, R. and Hallett, J.: Scavenging of soot particles by ice crystals, *Journal of Aerosol Science*, 21, S263–S266, [https://doi.org/10.1016/0021-8502\(90\)90234-O](https://doi.org/10.1016/0021-8502(90)90234-O), proceedings of the 1990 European Aerosol Conference, 1990.
- Peterson, D. A., Campbell, J. R., Hyer, E. J., Fromm, M. D., Kablick, G. P., Cossuth, J. H., and DeLand, M. T.: Wildfire-driven thunderstorms cause a volcano-like stratospheric injection of smoke, *npj Clim Atmos Sci*, <https://doi.org/10.1038/s41612-018-0039-3>, 2018.
- Peterson, D. A., Fromm, M. D., McRae, R. H. D., Campbell, J. R., Hyer, E. J., Taha, G., Camacho, C. P., Kablick, G. P., Schmidt, C. C., and DeLand, M. T.: Australia’s Black Summer pyrocumulonimbus super outbreak reveals potential for increasingly extreme stratospheric smoke events, *npj Clim Atmos Sci*, <https://doi.org/10.1038/s41612-021-00192-9>, 2021.
- PollyNET(2023): PollyNET lidar data base, available at: <http://polly.tropos.de/>, last access: 27 March, 2023.
- Radenz, M., Bühl, J., Seifert, P., Baars, H., Engelmann, R., Barja González, B., Mamouri, R.-E., Zamorano, F., and Ansmann, A.: Hemispheric contrasts in ice formation in stratiform mixed-phase clouds: disentangling the role of aerosol and dynamics with ground-based remote sensing, *Atmospheric Chemistry and Physics*, 21, 17 969–17 994, <https://doi.org/10.5194/acp-21-17969-2021>, 2021.
- Rieger, L. A., Randel, W. J., Bourassa, A. E., and Solomon, S.: Stratospheric temperature and ozone anomalies associated with the 2020 Australian New Year fires, *Geophysical Research Letters*, 48, <https://doi.org/10.1029/2021GL095898>, 2021.
- Rigg, Y. J., Alpert, P. A., and Knopf, D. A.: Immersion freezing of water and aqueous ammonium sulfate droplets initiated by humic-like substances as a function of water activity, *Atmospheric Chemistry and Physics*, 13, 6603–6622, <https://doi.org/10.5194/acp-13-6603-2013>, 2013.
- Rolph, G., Stein, A., and Stunder, B.: Real-time Environmental Applications and Display sYstem: READY, *Environmental Modelling & Software*, 95, 210–228, <https://doi.org/10.1016/j.envsoft.2017.06.025>, 2017.
- Safford, H. D., Paulson, A. K., Steel, Z. L., Young, D. J. N., and Wayman, R. B.: The 2020 California fire season: A year like no other, a return to the past or a harbinger of the future?, *Global Ecology and Biogeography*, 31, 2005–2025, <https://doi.org/https://doi.org/10.1111/geb.13498>, 2022.
- Santachiara, G., Piazza, M., and Belosi, F.: Aerosol scavenging during the early growth stage of ice crystal formation, *Atmospheric and Climate Sciences*, 8, 395–409, <https://doi.org/10.4236/acs.2018.84026>, 2018.
- Schill, G. P., Froyd, K. D., Bian, H., Kupc, A., Williamson, C., Brock, C. A., Ray, E., Hornbrook, R. S., Hills, A. J., Apel, E. C., Chin, M., Colarco, P. R., and Murphy, D. M.: Widespread biomass burning smoke throughout the remote troposphere, *Nat. Geosci.*, 13, 422–427, <https://doi.org/10.1038/s41561-020-0586-1>, 2020.
- Schumann, U., Mayer, B., Gierens, K., Unterstrasser, S., Jessberger, P., Petzold, A., Voigt, C., and Gayet, J.-F.: Effective Radius of Ice Particles in Cirrus and Contrails, *Journal of the Atmospheric Sciences*, 68, 300 – 321, <https://doi.org/10.1175/2010JAS3562.1>, 2011.
- Seifert, P., Ansmann, A., Mattis, I., Wandinger, U., Tesche, M., Engelmann, R., Müller, D., Pérez, C., and Hausteine, K.: Saharan dust and heterogeneous ice formation: Eleven years of cloud observations at a central European EARLINET site, *Journal of Geophysical Research: Atmospheres*, 115, <https://doi.org/10.1029/2009JD013222>, 2010.
- Seifert, P., Ansmann, A., Groß, S., Freudenthaler, V., Heinold, B., Hiebsch, A., Mattis, I., Schmidt, J., Schnell, F., Tesche, M., Wandinger, U., and Wiegner, M.: Ice formation in ash-influenced clouds after the eruption of the Eyjafjallajökull volcano in April 2010, *Journal of Geophysical Research: Atmospheres*, 116, <https://doi.org/https://doi.org/10.1029/2011JD015702>, 2011.
- Stein, A. F., Draxler, R. R., Rolph, G. D., Stunder, B. J. B., Cohen, M. D., and Ngan, F.: NOAA’s HYSPLIT Atmospheric Transport and Dispersion Modeling System, *Bulletin of the American Meteorological Society*, 96, 2059–2077, <https://doi.org/10.1175/BAMS-D-14-00110.1>, 2015.

- Thomas, L., Cartwright, J. C., and Wareing, D. P.: Lidar observations of the horizontal orientation of ice crystals in cirrus clouds, *Tellus B*, 42, 211–216, <https://doi.org/10.1034/j.1600-0889.1990.00001.x-i1>, 1990.
- Torres, O., Jethva, H., Ahn, C., Jaross, G., and Loyola, D. G.: TROPOMI aerosol products: evaluation and observations of synoptic-scale carbonaceous aerosol plumes during 2018–2020, *Atmospheric Measurement Techniques*, 13, 6789–6806, <https://doi.org/10.5194/amt-13-6789-2020>, 2020.
- Vaughan, G., Draude, A. P., Ricketts, H. M. A., Schultz, D. M., Adam, M., Sugier, J., and Wareing, D. P.: Transport of Canadian forest fire smoke over the UK as observed by lidar, *Atmospheric Chemistry and Physics*, 18, 11 375–11 388, <https://doi.org/10.5194/acp-18-11375-2018>, 2018.
- Veselovskii, I., Hu, Q., Ansmann, A., Goloub, P., Podvin, T., and Korenskiy, M.: Fluorescence lidar observations of wildfire smoke inside cirrus: a contribution to smoke–cirrus interaction research, *Atmospheric Chemistry and Physics*, 22, 5209–5221, <https://doi.org/10.5194/acp-22-5209-2022>, 2022.
- Wagner, R., Jähn, M., and Schepanski, K.: Wildfires as a source of airborne mineral dust – revisiting a conceptual model using large-eddy simulation (LES), *Atmospheric Chemistry and Physics*, 18, 11 863–11 884, <https://doi.org/10.5194/acp-18-11863-2018>, 2018.
- Wandinger, U.: Multiple-scattering influence on extinction- and backscatter-coefficient measurements with Raman and high-spectral-resolution lidars, *Appl. Opt.*, 37, 417–427, <https://doi.org/10.1364/AO.37.000417>, 1998.
- Wang, B. and Knopf, D. A.: Heterogeneous ice nucleation on particles composed of humic-like substances impacted by O<sub>3</sub>, *Journal of Geophysical Research: Atmospheres*, 116, <https://doi.org/10.1029/2010JD014964>, 2011.
- Wang, B., Laskin, A., Roedel, T., Gilles, M. K., Moffet, R. C., Tivanski, A. V., and Knopf, D. A.: Heterogeneous ice nucleation and water uptake by field-collected atmospheric particles below 273 K, *Journal of Geophysical Research: Atmospheres*, 117, <https://doi.org/10.1029/2012JD017446>, 2012a.
- Wang, B., Lambe, A. T., Massoli, P., Onasch, T. B., Davidovits, P., Worsnop, D. R., and Knopf, D. A.: The deposition ice nucleation and immersion freezing potential of amorphous secondary organic aerosol: Pathways for ice and mixed-phase cloud formation, *Journal of Geophysical Research: Atmospheres*, 117, <https://doi.org/10.1029/2012JD018063>, 2012b.
- Yu, P., Toon, O. B., Bardeen, C. G., Zhu, Y., Rosenlof, K. H., Portmann, R. W., Thornberry, T. D., Gao, R.-S., Davis, S. M., Wolf, E. T., de Gouw, J., Peterson, D. A., Fromm, M. D., and Robock, A.: Black carbon lofts wildfire smoke high into the stratosphere to form a persistent plume, *Science*, 365, 587–590, <https://doi.org/10.1126/science.aax1748>, 2019.
- Zhao, B., Liou, K.-N., Gu, Y., Jiang, J. H., Li, Q., Fu, R., Huang, L., Liu, X., Shi, X., Su, H., and He, C.: Impact of aerosols on ice crystal size, *Atmospheric Chemistry and Physics*, 18, 1065–1078, <https://doi.org/10.5194/acp-18-1065-2018>, 2018.
- Zobrist, B., Marcolli, C., Pedernera, D. A., and Koop, T.: Do atmospheric aerosols form glasses?, *Atmospheric Chemistry and Physics*, 8, 5221–5244, <https://doi.org/10.5194/acp-8-5221-2008>, 2008.

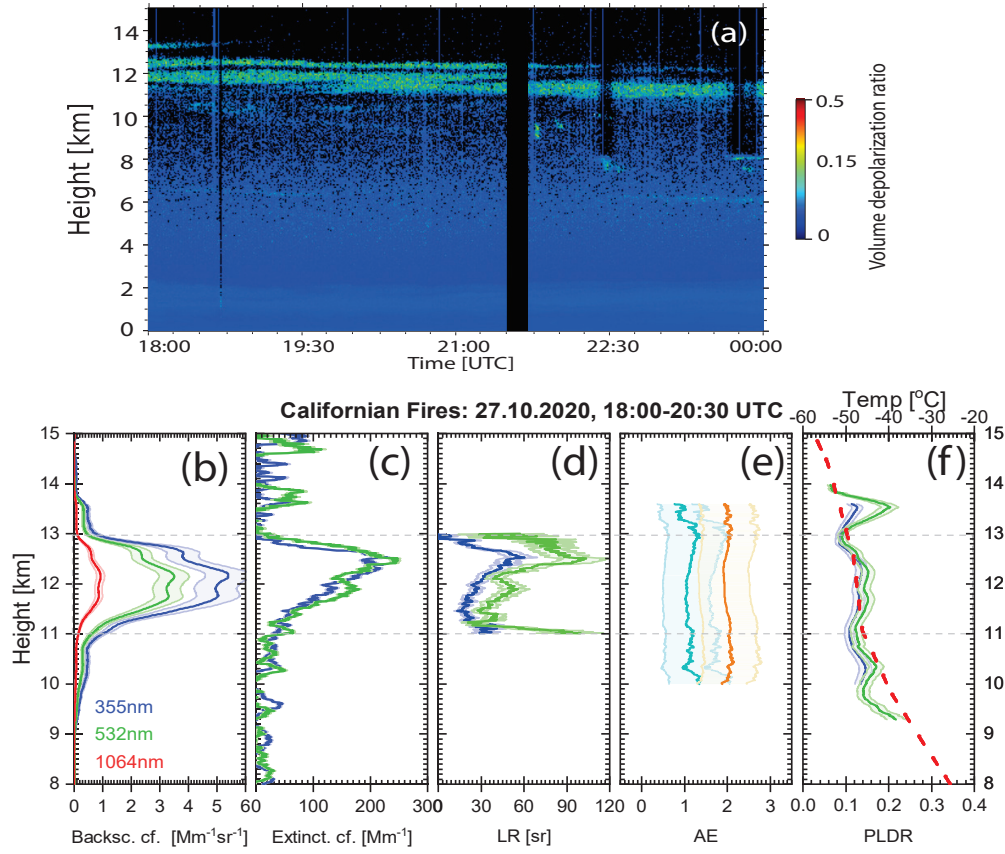


**Figure 1.** (a) Wildfire smoke layer between 11 and 13.5 km height over Limassol, Cyprus, on 27 October 2020, (b) particle backscatter coefficients at 355, 532, and 1064 nm, (c) extinction coefficients and (d) extinction-to-backscatter ratios (lidar ratios, LR) at 355 and 532 nm, (e) backscatter Ångström exponents (AE, blue for the 355-532 nm spectrum, orange for the 532-1064 nm spectrum), and (f) particle linear depolarization ratios (PLDR) at 355 and 532 nm and temperature profile with tropopause at 11 km (red, dashed line). 2.5-hour mean profiles (18:00-20:30 UTC) are shown in (b)-(f). Uncertainty margins are added. The uncertainties are about 15% (backscatter), 5-30% (extinction, lidar ratio), 50% (AE), and 10% (PLDR). Black vertical columns in (a) indicate periods with no measurements.

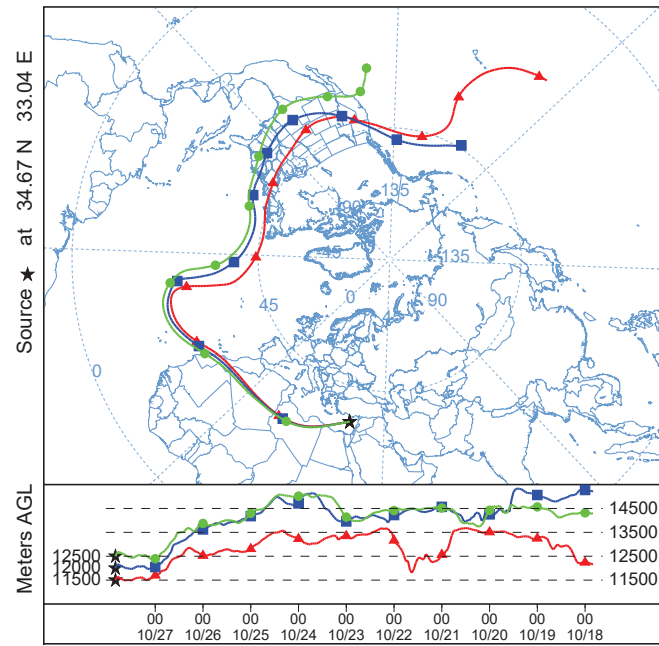


**Figure 2.** HYSPLIT 10 d backward trajectories arriving over Limassol, Cyprus (indicated by a star) on 27 October 2020, 20:00 UTC (HYSPLIT, 2023). Arrival heights are at 11500 m (red), 12000 m (blue), and 12500 m (green). Main smoke source region was California. The wildfire smoke was probably lofted by pyroCb convection into the upper troposphere (12-14.5 km height range).

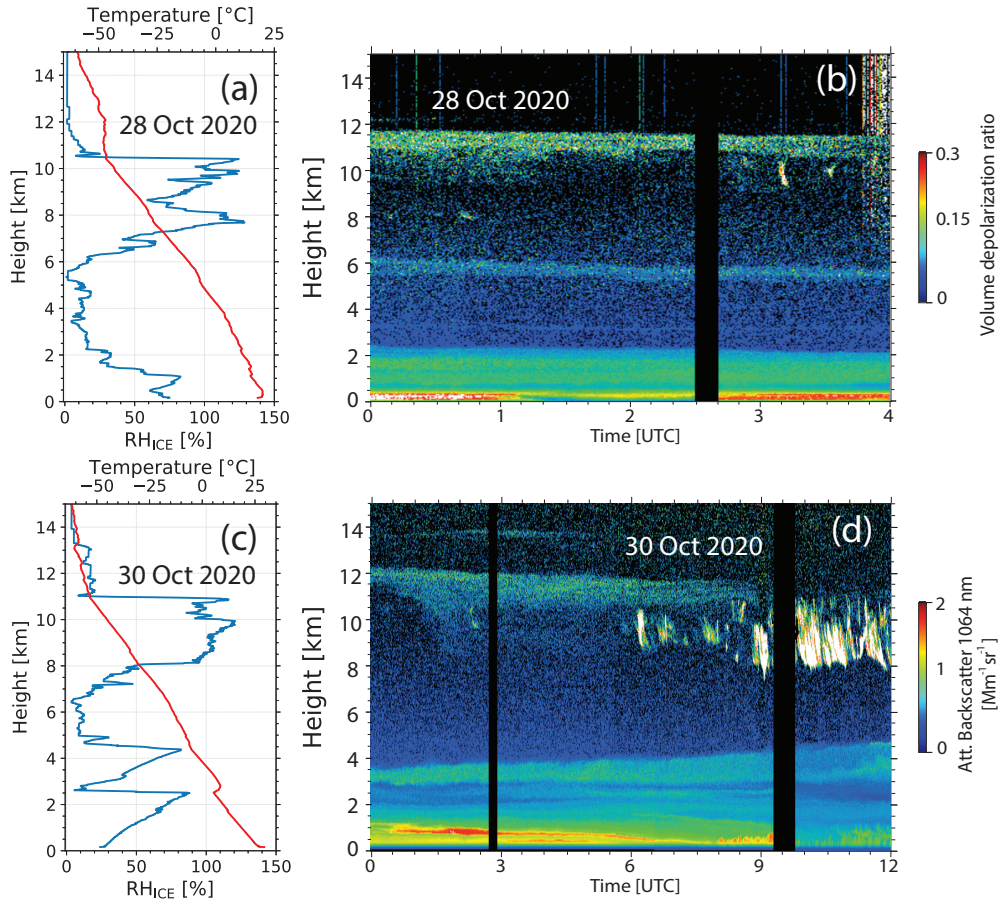


**Figure 3.** Formation of cirrus (white virga-like structures in panels a and b) in the lower part of an aged wildfire smoke layer (at 10–12.5 km height) on 28 October 2020 (a,b) and 30 October 2020 (c,d). In (a) and (c), radiosonde profiles of temperature (red) and relative humidity over ice (RH<sub>ICE</sub>, blue) are shown (radiosonde launches in (a) at 5 UTC and in (c) at 11 UTC). The sharp drop in the RH<sub>ICE</sub> profile at 10.5 km (a) and 11 km (c) indicates the tropopause. The time-height displays of the volume depolarization ratio (in b) and of the range-corrected 1064 nm backscatter signal (in d, equivalent to the 1064 nm attenuated backscatter coefficient) show smoke layers at 10–12 km and around 6 km (b) and 10–12.5 km and at 14 km height (d). Ice nucleation was most probably initiated at the top of the humid layer (close to the tropopause) at  $-47^{\circ}$  to  $-53^{\circ}\text{C}$ . Black vertical columns (in b and d, 0–15 km) indicate periods with no measurements.

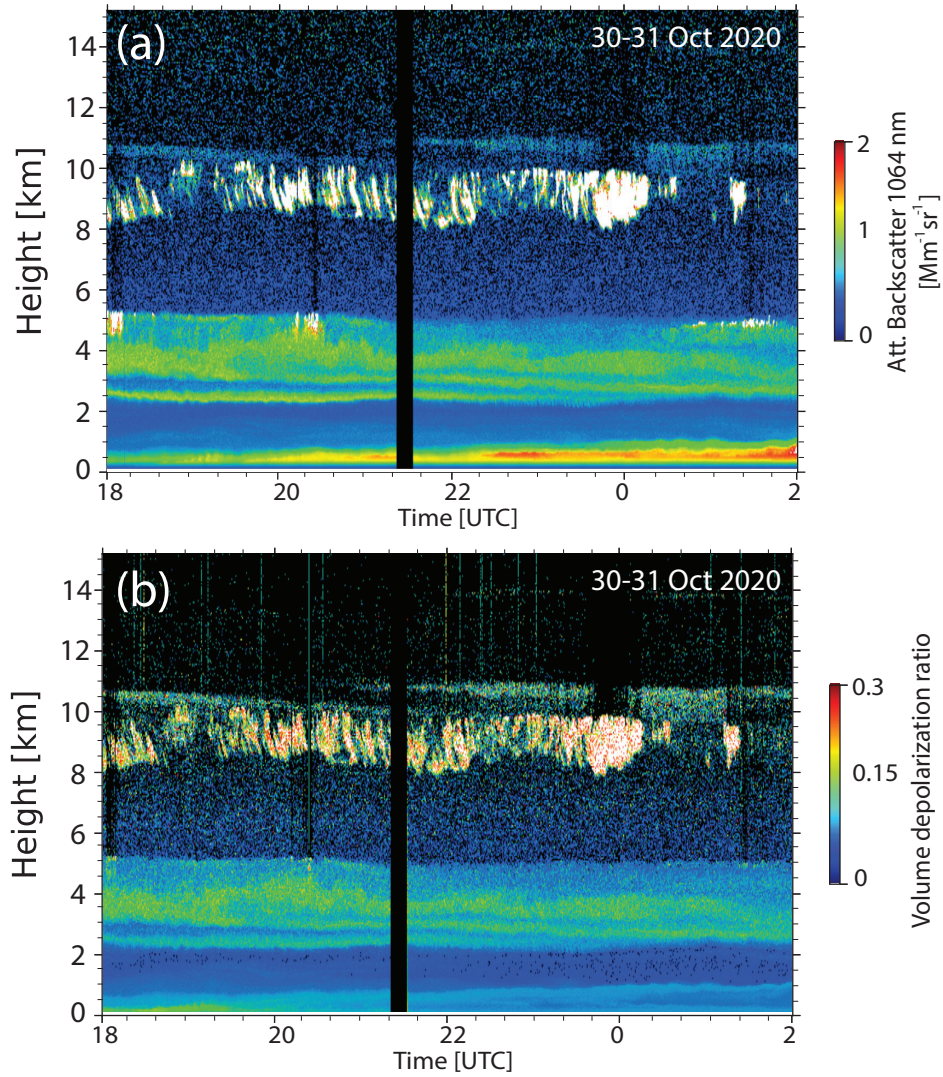


**Figure 4.** Same as Fig. 3b and d, except for 30-31 October 2020, 18:00-02:00 UTC. Ice nucleation is expected at the top of the ice virga zone (white features) and thus in lower part of the main smoke layers.



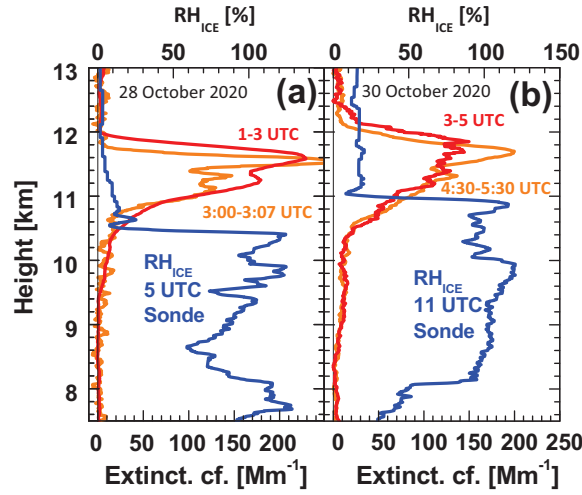


**Figure 5.** Wildfire smoke layers (orange and red particle extinction profiles) in the UTLS (orange: Klett solutions, 70 m vertical smoothing, red: Raman lidar solutions, 300 m signal smoothing) on (a) 28 and (b) 30 October 2020. The signal averaging periods are given in the panels. The 532 nm extinction coefficients are computed from the respective backscatter coefficients by multiplication with the smoke lidar ratio of 75 sr. The orange and red smoke layers partly overlap with the blue humid layers ( $RH_{ICE}$  profiles from radiosondes launched at 28 October, 5 UTC, and 30 October, 11 UTC). The top height of the humid layer at 10.5 km (a) and 11 km (b) indicates the tropopause. Most favorable ice nucleation conditions are given just below the tropopause, i.e., in the coldest region of the troposphere.

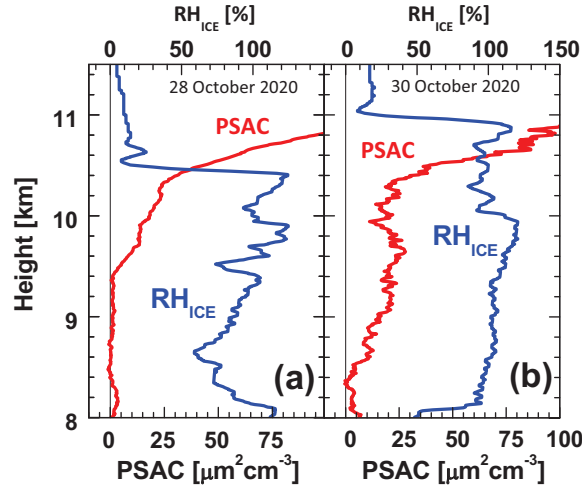


**Figure 6.** Same as Fig. 5, except for the particle surface area concentration (PSAC, red profiles). The extinction coefficients (red Raman lidar profiles) in Fig. 5 were converted into PSAC profiles by using Eq. (1) in Sect. 3. A clear overlap of the red smoke layers with the blue cirrus generation zone ( $RH_{ICE}$  profile) from 9.5 km (a) and 8.5 km (b) up to the tropopause (top of the humid layer) is visible.

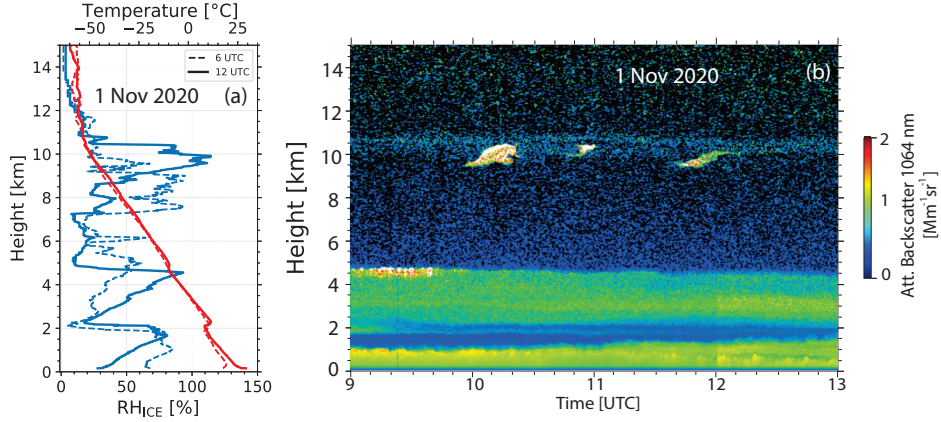


**Figure 7.** Observation of gravity-wave-induced cirrus formation in wildfire smoke on 1 November 2020. (a) Radiosonde profiles (launches at 5 and 11 UTC) of temperature (red) and relative humidity over ice,  $RH_{ICE}$  (blue), (b) time-height display of lidar observations of the ice clouds (wave-like white features around 10 km and 12 UTC) and the smoke layer from 10-11 km height. The sharp drop in the  $RH_{ICE}$  profile at 10.5 km (a, 12 UTC) indicates the tropopause. The time-height display of the range-corrected 1064 nm backscatter signal (denoted as attenuated backscatter) shows the smoke layer, the ice clouds, as well as a pronounced Saharan dust layer (2-5 km height) and the local boundary layer (up to about 1-1.5 km height).

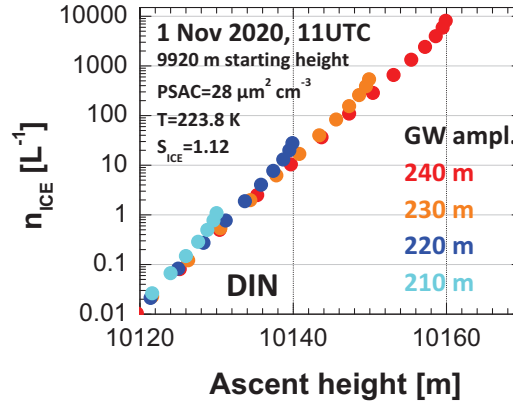


**Figure 8.** Accumulated ice crystal number concentration,  $n_{ICE}$ , as function of ascent height above the starting height of 9920 m. The gravity-wave-induced lofting of an air parcel is simulated. Initial  $T$  and  $S_{ICE}$  values (at 9920 m height according to the radiosonde launched on 1 November 2020, 11 UTC) are given in the panel. Simulation resolution is  $\Delta t = 10$  s. Four simulations with different lofting amplitudes of 210 m (maximum height, reached after 295 s,  $S_{ICE} = 1.40$  at this height), 220 m (reached after 310 s,  $S_{ICE} = 1.41$ ), 230 m (reached after 324 s,  $S_{ICE} = 1.43$ ), and 240 m (reached after 338 s,  $S_{ICE} = 1.44$ ) are shown. Updraft speed was around  $0.7 \text{ m s}^{-1}$ . Lofting by about 220 m is obviously sufficient to activate around 20-50 INPs per L<sup>-1</sup>. Lofting by 230-240 m leads to unrealistically high ice crystal number concentrations of about 800 to 9000 L<sup>-1</sup> in the simulations.



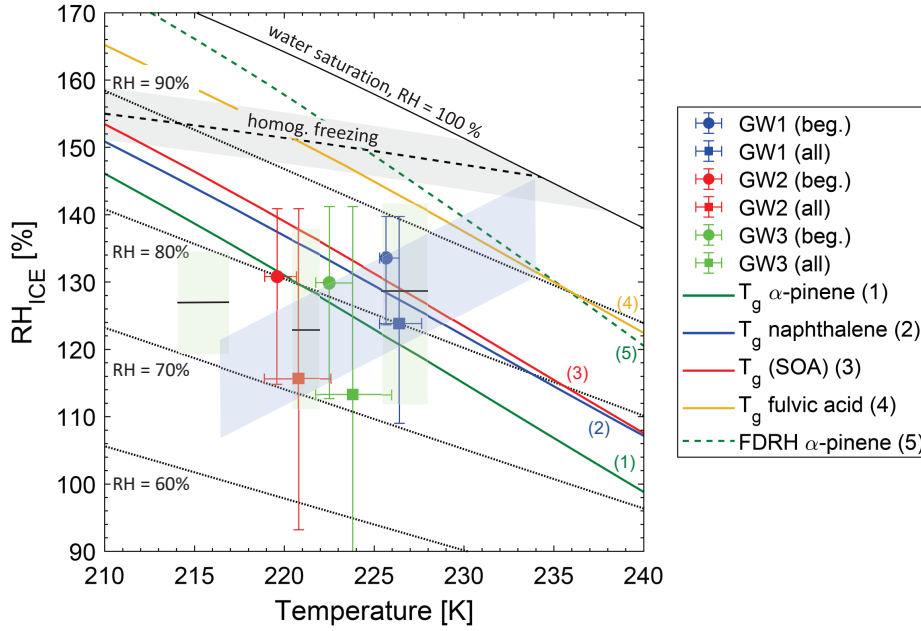


**Figure 9.** Thermodynamic conditions of observed gravity-wave (GW)-induced cirrus cloud formation (blue, red, and green symbols and bars represent events of 28 October (GW1), 30 October (GW2), and 1 November (GW3), respectively) in comparison to homogeneous (grey area with dashed black line) and heterogeneous ice nucleation (greenish area with horizontal bar), phase transitions of organic particles (colored and numbered lines), and continental cirrus conditions (bluish area). Circles (mean values) and bars (range of values) represent the initial loft phase of 300-400 s (beg.) and squares and bars the entire GW period (all). The black solid line represents conditions of water saturation (100% RH). Dotted lines indicate constant relative humidity over water (90 to 60% RH from top to bottom, respectively). The dashed line and grey shading represent the homogeneous freezing limit for droplets of 10  $\mu\text{m}$  in size and corresponding uncertainty (Koop et al., 2000; Koop, 2004). Greenish areas and horizontal lines represent the range and mean conditions of observed deposition ice nucleation by leonardite particles (Wang and Knopf, 2011) serving as surrogate of organic ice-nucleating particles. The glass transition temperature  $T_g$  (molecular mobility is frozen for  $T < T_g$ ) of laboratory generated  $\alpha$ -pinene SOA (green line or 1, Charnawskas et al. (2017)), naphthalene SOA (blue line or 2, Charnawskas et al. (2017)), field-derived SOA (red line or 3, (Wang et al., 2012b)), and Suwannee River Fulvic Acid particles (orange or 4, (Wang et al., 2012b)) are plotted. The dashed green line (or 5) displays the full deliquescence RH (FDRH) for  $\alpha$ -pinene SOA particles, 500 nm in diameter, for a humidification rate simulating an updraft of 1  $\text{m s}^{-1}$  (Charnawskas et al., 2017). The light blue area indicates the range of observed conditions of continental orographic wave clouds and cirrus (Heymsfield and Miloshevich, 1995).

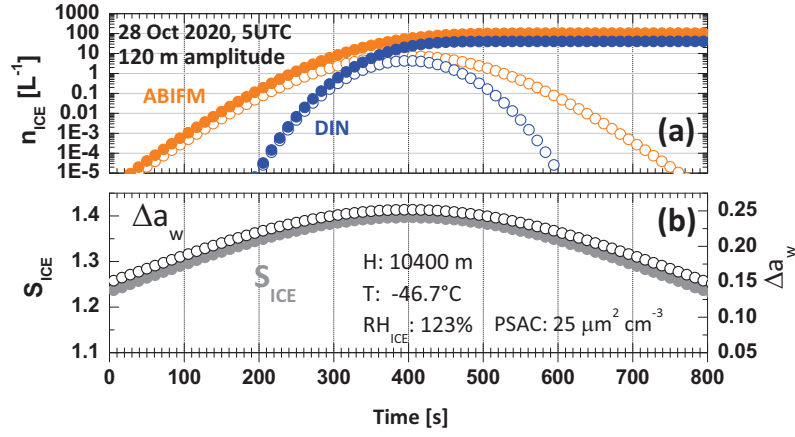


**Figure 10.** (a) Simulation of the nucleation of ice crystals ( $n_{ICE}$ ) during the ascent phase (first 800 s, from the starting height at 10400 m to amplitude maximum and back to the starting height level) of a gravity wave with an amplitude of 120 m. Temperature ( $T$ ) and  $RH_{ICE}$  conditions as observed with Nicosia radiosonde on 28 October 2020 (launch at 5 UTC) at the GW starting height  $H$  are given in panel (b) together with the simulated PSAC values (from the lidar observations). Immersion freezing (ABIFM) as well as deposition ice nucleation (DIN) parameterizations are applied to compute  $n_{INP} = n_{ICE}$  as described in Sect. 3.1. Simulation resolution is 10 s. Open circles (in a) show nucleated ice crystals within each simulation step width of  $\Delta t = 10$  s, and closed circles the accumulated number concentration of all freshly nucleated ice crystals. (b) Evolution of the ice supersaturation  $S_{ICE}$  (closed gray circles) and the water activity criterion  $\Delta a_w$  (open circles, Eq. 3) during the lofting period. The simulation belongs to the observations in Figs. 3a and b and 6a.